PAPER

Optimising photovoltaic modules for indoor energy-harvesting systems

Austin M Kay[1,*] ⓘ, Shimra N Ahmed[1] ⓘ, Nicholas Burridge[1] ⓘ, Drew B Riley[1] ⓘ, Ardalan Armin[1] ⓘ, Oskar J Sandberg[2] ⓘ, Zaid Haymoor[3] ⓘ, Matthew J Carnie[3] ⓘ, Paul Meredith[1] ⓘ and Gregory Burwell[1,*] ⓘ

1 Sustainable Advanced Materials (Sêr-SAM), Centre for Integrative Semiconductor Materials (CISM), Department of Physics, Swansea University Bay Campus, Swansea, SA1 8EN, United Kingdom
2 Physics, Faculty of Science and Engineering, Åbo Akademi University, 20500 Turku, Finland
3 Department of Materials Science and Engineering, Faculty of Science and Engineering, Swansea University Bay Campus, Swansea SA1 8EN, United Kingdom
* Authors to whom any correspondence should be addressed.

E-mail: a.m.kay.954708@swansea.ac.uk and g.burwell@swansea.ac.uk

Abstract

By harvesting low-intensity ambient light, indoor photovoltaics (PVs) could soon power countless internet-of-things (IoT) devices and sensors. However, indoor illumination conditions vary from room to room and even hour to hour, leading to inconsistent PV power generation. To overcome this, energy-harvesting circuitry can be used alongside indoor PV modules to recharge batteries or capacitors, forming energy-harvesting systems that enable consistent discharge into IoT devices. The optimisation of such systems is a topic of intense research. In this work, we use thermodynamic principles to model power generation in indoor PV modules based on inorganic, perovskite, and organic semiconductors, before evaluating the efficiency of the whole energy-harvesting system. In these investigations, we account for detailed device physics, including sub-gap absorption, band-filling effects, point defects, and parasitic resistances, while also considering performance under several different light sources. Ultimately, we find that the maximum power point voltage (V_{mpp}) is pivotal in determining the optimal number of cells for an indoor PV module. Despite some PV materials having a lower V_{mpp} due to narrower bandgaps or increased voltage losses, we find that this can be compensated for by increasing the number of cells; though too many cells can actually lead to inefficient energy harvesting. As a final case study, we evaluate the power generated and stored in a typical day (where an interplay between daylight and artificial light is present) to determine how stored energy translates to measurements made with an IoT device.

1. Introduction

As part of the Fourth Industrial Revolution that's currently evolving the global technological landscape, wireless devices and sensors are being widely deployed to form the Internet-of-Things (IoT) [1]. These IoT devices include remote sensors for temperature, carbon dioxide levels, humidity, and more [2, 3]. However, this accelerating deployment will bring a considerable demand for energy that must be met in a sustainable, environmentally-friendly, and economically-viable manner. To this end, innovative approaches are required to provide locally-generated, clean energy.

One technological advancement that could bring power to IoT devices deployed in internal spaces—such as offices and homes—are indoor photovoltaics (PVs), which negate the need for disposable batteries [4]. Indoor PVs need not be as large as solar panels; with device areas on the order of just $30\,\mathrm{cm}^2$ being ample for powering most IoT devices [5]. However, powering IoT devices directly with indoor PVs is impractical due the variability in available light resource throughout the day. To overcome this and extend operating periods,

IoT systems commonly employ a 'harvest-store-use' architecture [6], wherein the indoor PVs recharge batteries or supercapacitors in a process mediated by an energy-harvesting board (EHB). The stored power is then discharged into the IoT device as and when required. However, the harvest-store-use process is not 100% efficient. Firstly, the PV device does not convert all the incident light to electricity; it instead generates power at some power conversion efficiency (PCE). Following this, the EHB stores the generated power at efficiency η_{EHB} —which can depend on both the voltage (V) and current (I) flowing through the circuit [7]. The net result of these processes is the system efficiency (η_{sys}), which quantifies how much of the incident light power is stored by the energy-harvesting system and then made available to the IoT device; it is defined as

$$\eta_{sys} = [PCE \times \eta_{EHB}] \times \eta_{dis}. \tag{1}$$

Here, η_{dis} is the efficiency of the discharging of power into the IoT device, which will depend on the exact IoT device being used. In this work, we remain agnostic to any IoT device-specific discharge efficiency and focus solely on the efficiency of the energy-harvesting system—shown in square brackets in equation (1)—by effectively assuming $\eta_{dis} = 1$. Setting the EHB aside for now, there are two main considerations for optimising the system efficiency: (i) the available light resource and (ii) the intrinsic losses of the PV device.

To power IoT devices in indoor settings, indoor PVs harvest low-intensity, ambient light. As many different light sources can be present indoors, the spectral lineshape and intensity of this light can vary from one room to the next, and even between locations in the same room [8, 9]. This makes it challenging to predict the real-world performance of indoor PVs. Compounding this is the difficulty in making laboratory-scale comparisons in the absence of widely-adopted indoor PV testing standards. Different laboratories commonly use different light sources, and the spectral lineshape of the light can also be influenced by the attenuation method used to reduce it to a desired intensity, with neutral density filters and prism attenuator approaches being particularly problematic [10]. Highly-engineered approaches are required to overcome this, such as the use of digital-micromirror devices [11]. Complicating things further is the use of photometric units of illuminance (lux) to measure light intensity, which in the context of different light sources leads to variations in irradiance. In simpler terms, this means that sources that are perceived to be equally bright can actually have different light intensities. Testing standards alleviate some of these difficulties, with indoor PV testing standard IEC TS 62 607-7-2:2023 recently being published to this end [12–14].

Under most sources of artificial, visible light, PV materials require optical gaps (E_{opt}) between 1.7 eV and 1.9 eV to achieve high PCEs [15–17]. Next-generation semiconductor materials with wide, tuneable gaps are therefore desirable for indoor PV applications, with the ever-improving perovskites and organic semiconductors being of particular relevance [18–22]. These materials are solution-processible and flexible, enabling the fabrication of large-area PVs using low-temperature, low embodied energy techniques like roll-to-roll printing and blade coating [23–26]. Despite these advantages, perovskite and organic PVs have limitations at both the material and the device level.

At the material level, the performance of next-generation semiconductors is limited by intrinsic loss mechanisms. These include (radiative) losses in the open-circuit voltage (V_{oc}) induced by sub-gap absorption, manifested by so-called Urbach tails encountered in a wide range of semiconductor materials, including inorganic systems like amorphous silicon and cadmium telluride (CdTe), as well as perovskites and organic semiconductors [17, 27, 28]. Further losses to the open-circuit voltage arise from non-radiative recombination. In organic PVs, this non-radiative open-circuit voltage loss has been observed to decrease with increasing E_{opt} via the energy-gap law [29]. Improvements in material combinations are constantly reducing these losses, however, and thus gradually increasing device performance. A notable material-level evolution for organic PVs has been the transition from fullerene to non-fullerene acceptor (NFA) molecules boosting PCEs to 20% in recent years [21, 30–33].

Following the optimisation of materials, the next important question is how the performance of laboratory-scale devices translates to large-area devices ($>10\,cm^2$). At such scales, the PCE can become limited by parasitic shunt resistances, including the intrinsic, bulk shunt resistance of the material and the shunt resistance of point defects that form during imperfect deposition procedures [5, 34]. At low light intensities, Ohmic losses attributed to the series resistance of electrodes are small (due to the low current densities), whereas shunt resistances play a more important role. To increase the effective shunt resistance of the device while also increasing voltage, monolithic PV cells can be converted/singulated into PV modules consisting of pixels interconnected in series using patterning techniques such as laser scribing [35–37].

Herein, we extend prior work on the thermodynamic limits of indoor PV performance while accounting for different loss mechanisms in photovoltaic devices [17], including transport losses, sub-gap absorption, and parasitic resistances induced by point defects. In these investigations, we utilize light-emitting diode

(LED)-B4 as a light source, as specified in indoor PV testing standard IEC TS 62 607-7-2:2023 [12–14]. Following this, we use the PV external quantum efficiency (EQE_{PV}) spectra of real devices to demonstrate how the design of PV modules can influence the performance of energy-harvesting systems. In these investigations, we consider the e-peas® AEM13920 EHB (a popular choice for IoT systems) [7]. We find that the optimal number of cells in a PV module will closely depend on both the material type and operational light intensity range. We probe the sensitivity of these devices to changes in light source, before presenting a case study on the power stored by energy-harvesting systems based on different PV devices, using irradiance spectra for a typical day [9]. To support these findings, we have upgraded our open-source computational tool, PV-Simulator [38], with capabilities for simulating energy-harvesting systems while expanding its database to include more than 300 state-of-the-art PV devices [39], including inorganic, perovskite, and organic PVs.

2. Single-cell photovoltaics

Before focussing on the optimisation of indoor PV modules for indoor energy-harvesting applications, we first establish concepts relevant to the optimisation of the individual PV cells that form a module. We start by exploring the diverse illumination conditions that indoor PVs may encounter, which can impact power generation and have far-reaching implications for module optimisation. Following this, we present idealised limits for power generation in common PV materials—including inorganics, perovskites, and organics—thereby conveying what performance is achievable despite intrinsic loss mechanisms. We then apply PV-Simulator's open-source database—which contains the spectral responses of hundreds of state-of-the-art devices—to predict realistic device performance, before probing the detrimental effects of shunt resistance. Finally, we investigate how versatile devices can be with respect to the many different light sources present in typical indoor environments.

2.1. Light resource availability for energy-harvesting systems

To provide locally generated power for consumer electronics and IoT devices, energy-harvesting systems based on PV modules harvest low-intensity ambient light. As previously indicated, such systems typically employ the harvest-store-use architecture illustrated in figure 1(a), with the output of the PV device (be it a cell or module) being stored in a battery/capacitor by an intermediary EHB [6, 40]. As we explore in section 3 using the e-peas® AEM13920 as an exemplar EHB [7], the efficiency of this energy-harvesting process depends on the PV device's maximum power point voltage (V_{mpp}) and current (I_{mpp}). In turn, these parameters depend on the intensity and spectral distribution of the incident light [17], meaning that the optimisation of PV devices for energy-harvesting applications requires some foresight of possible deployment locations and their associated lighting conditions.

In practice, indoor energy-harvesting systems could encounter light emitted by all manner of sources including LEDs, fluorescent lamps (FL), the Sun, or some superposition of multiple sources [9]. Without the widespread adoption of a robust indoor PV testing standard, this multitude of light sources makes meaningful comparisons between different laboratories a challenge. Recently, indoor PV testing standard IEC TS 62 607-7-2:2023 was introduced to alleviate some of these issues [12–14]. Figure 1(b) shows the spectral irradiances (I_{source}) of the International Commission on Illumination's (CIE's) LED-B4 and FL-10 light sources specified in this testing standard, which are plotted against the photon energy (E). Note that these spectra were plotted at an illuminance $L_{source} = 1000$ lux, with the conversion from the radiometric units of irradiance (physical light intensity) to the photometric units of illuminance (perceived brightness) made using

$$L_{source} = L_0 \int_{1.77}^{3.35} \nu(E)\, I_{source}(E)\, dE, \tag{2}$$

with $\nu(E)$ being the luminous efficiency of photopic vision and $L_0 = 6830\,\text{lux}/\left(\text{mW cm}^{-2}\right)$ [42, 43]. A full list of symbols and abbreviations is provided in supplementary note 1. For reference, figure 1(b) also contains the AM1.5 G solar spectrum scaled down to 1000 lux using the overlap integral in equation (2), illustrating how the Sun's irradiance spectrum is broader and red-shifted compared to the LED-B4 and FL-10 spectra. From this figure, it is clear that different light sources can have vastly different spectral irradiances while having the same illuminance,

Of course, focussing on just one or two light sources neglects the diverse illumination conditions encountered in real deployment locations. For example, the irradiance spectra of incandescent lights (modelled as black-body emitters at a given colour temperature) and typical LED light sources are illustrated
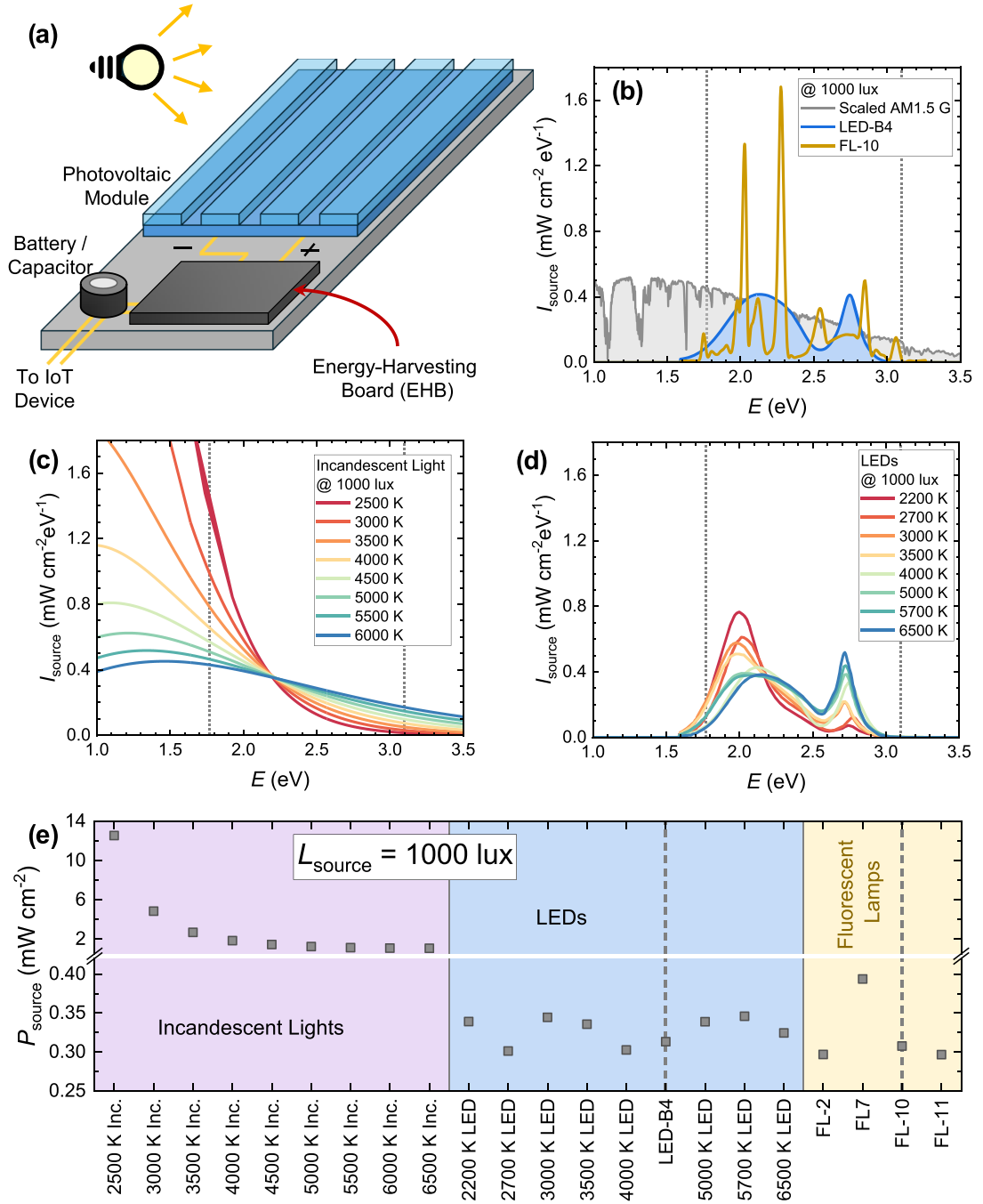
Figure 1. Light resource considerations for energy-harvesting systems. (a) Illustration of a typical energy-harvesting system, including a photovoltaic module that converts ambient light to electrical power, which is stored in a battery/supercapacitor by an energy-harvesting board (EHB) at efficiency η_{EHB}. (b) Spectral irradiance (I_{source}) versus photon energy (E) for two light sources specified in indoor PV standard IEC TS 62 607-7-2:2023 [12–14]. Namely, these are the LED-B4 and FL-10 spectra, which are here scaled to an illuminance $L_{source} = 1000$ lux. Included for reference is the AM1.5 G solar spectrum scaled to $L_{source} = 1000$ lux according to the overlap integral given in equation (2). Additionally, the spectral irradiances of (c) incandescent light bulbs (modelled as black-body emitters) and (d) LEDs of a variety of colour temperatures are indicated at $L_{source} = 1000$ lux [41]. (e) Corresponding irradiances ($P_{source} = \int_0^\infty I_{source}(E)\,dE$) of a variety of visible light sources, with all having illuminance $L_{source} = 1000$ lux.

in figures 1(c) and (d) [41], respectively, where all spectra hold the same illuminance ($L_{source} = 1000$ lux). From these graphs, it is clear that spectral irradiance can differ greatly with apparent colour temperature; with the peak at high (low) photon energies increasing (decreasing) as colour temperature increases. For example, if one measured the PCE of a device with bandgap $E_{opt} = 2.2$ eV under a (warm white) 2700 K LED at a given illuminance and then measured the same device under a (cool white) 5700 K LED at the same illuminance, then the two measurements would be made at very different irradiances. This is clarified in

figure 1(e), wherein the integrated irradiances (P_{source}) of different sources scaled to an illuminance $L_{\text{source}} = 1000\,\text{lux}$ have been quantified from the spectral irradiances and compared using

$$P_{\text{source}} = \int_0^{\infty} I_{\text{source}}(E)\,\mathrm{d}E. \tag{3}$$

From this figure, it is clear that P_{source} varies by more than 33% for different LEDs and FL despite the sources having the same L_{source}. These variations are up to two orders-of-magnitude for conventional incandescent lights. Consequently, while permissible in the context of a singular light source, photometric units of illuminance are not reliable when considering the performance of physical systems under different sources, and they might ultimately lead to inaccuracies in PV device characterisation. We note that similar conclusions on the unreliability of lux measurements have been drawn in the past [16, 44, 45]. In the remainder of this work, we therefore use the radiometric units of irradiance and spectral irradiance, with the photometric units of illuminance only provided for comparison where necessary.

2.2. Thermodynamic limits of single cells in idealised device models

To provide context for results presented using real PV devices in the next section, we now summarise an investigation on the thermodynamic performance limits of idealised PV cells based on different material classes [17]. In this investigation, the PV figures-of-merit were evaluated by relating the current density (J) generated by a PV cell to the voltage bias (V) across it using the diode equation [17, 46]

$$J(V) = J_0\left(V_{\text{drop}}\right) \times \left[\exp\left(\frac{qV_{\text{drop}}}{k_{\text{B}}T}\right) - 1\right] + \frac{V_{\text{drop}}}{R_{\text{p}}} - J_{\text{ph}}. \tag{4}$$

Here, q is the elementary charge, k_{B} is the Boltzmann constant, and T is the temperature. The effective voltage drop across the device (V_{drop}) relates to the voltage bias via $V_{\text{drop}} = V - A_{\text{cell}}R_{\text{s}}J(V)$, with A_{cell} and R_{s} being the cell's cross-sectional area and total external series resistance (induced by electrodes, wires, etc.), respectively. On the other hand, R_{p} denotes the parallel (total shunt) resistance of the cell, which can include contributions from point defects [34]. The spectral response of the PV cell enters equation (4) via the calculation of the photocurrent density (J_{ph}) and dark saturation current density (J_0), which can be written in terms of the EQE_{PV} as [17, 27, 47]

$$J_{\text{ph}}\left(V_{\text{drop}}\right) = q \int_0^{\infty} \text{EQE}_{\text{PV}}(E) \tanh\left(\frac{E - qV_{\text{drop}}}{4k_{\text{B}}T}\right) \Phi_{\text{source}}(E)\,\mathrm{d}E, \tag{5}$$

and

$$J_0\left(V_{\text{drop}}\right) = \frac{q}{\text{EQE}_{\text{EL}}} \int_0^{\infty} \text{EQE}_{\text{PV}}(E)\, w\left(E, V_{\text{drop}}\right) \Phi_{\text{Planck}}(E)\,\mathrm{d}E, \tag{6}$$

respectively. Therein, $\Phi_{\text{source}}(E) = I_{\text{source}}(E)/E$ is the spectral photon flux of the light source, while $\Phi_{\text{Planck}}(E) = \frac{2\pi E^2}{h^3 c^2} \times \left[\exp\left(\frac{E}{k_{\text{B}}T}\right) - 1\right]^{-1}$ is the spectral photon flux of thermal radiation for a cell at temperature T. In equation (6), EQE_{EL} is the cell's electroluminescent external quantum efficiency (equal to unity in the radiative limit), whereas $w\left(E, V_{\text{drop}}\right)$ denotes a voltage-dependent correction factor that accounts for band-filling effects and the chemical potential of radiation [17, 27, 48]; it is defined by

$$w\left(E, V_{\text{drop}}\right) \equiv \frac{1}{\left[1 + \exp\left(\frac{qV_{\text{drop}} - E}{2k_{\text{B}}T}\right)\right]^2}. \tag{7}$$

In idealised models, these equations can be solved analytically to yield the PV figures-of-merit [17]. Though in general, these equations are solved numerically to identify V_{mpp} and the maximum power point current density (J_{mpp}) of a PV cell, with its PCE ultimately being calculated using

$$\text{PCE} = \frac{V_{\text{mpp}}\left|J_{\text{mpp}}\right|}{P_{\text{source}}}. \tag{8}$$

Using equations (4)–(8), the PV figures-of-merit can be modelled for any PV cell using its EQE_{PV} spectrum, EQE_{EL} value, and parasitic resistances.

The technique outlined above is used throughout this work to model power generation per unit area of a PV device, and we first apply it in three idealised models. In these models, parasitic resistances are assumed to have no effect ($R_s = 0$ and $R_p \rightarrow \infty$), such that other intrinsic losses present in the PV cells in the thermodynamic limit can be audited. The first of these models is the Shockley-Queisser (SQ) model—a valid upper limit for PV device performance where transport and non-radiative losses are assumed negligible, while the material has perfectly-defined band edges (i.e. no sub-gap absorption) [49]. In the SQ model, EQE_{PV} is a step function about a threshold optical gap (E_{opt}):

$$EQE_{PV}(E) = \begin{cases} 1, & \text{if } E \geq E_{opt}, \\ 0, & \text{otherwise} \end{cases}. \tag{9}$$

An example EQE_{PV} spectrum in the SQ model is illustrated by the black curve in figure 2(a), with a discontinuous step in absorption at $E_{opt} = 1.5\,eV$.

While the SQ model can provide an upper limit and identify optimal bandgaps, its underlying assumption of perfectly-defined band edges neglects subtleties present in real devices. This includes the effects of thermal broadening and energetic disorder, which in most materials lead to an exponential decay in EQE_{PV} below the gap known as a 'sub-gap' or 'Urbach' tail [28, 50–56]. Such Urbach tails are important as they detrimentally affect device performance by inducing losses in the radiative open-circuit voltage (V_{oc}^{rad}) [17]. To account for this effect, EQE_{PV} can be modelled as

$$EQE_{PV}(E) = EQE_{max} \times \begin{cases} 1, \text{if } E \geq E_{opt}, \\ \exp\left(\frac{E - E_{opt}}{E_U}\right), \text{otherwise} \end{cases}. \tag{10}$$

Here, E_U is the characteristic Urbach energy of the sub-gap tail, whereas EQE_{max} is the above-gap quantum efficiency, with $EQE_{max} < 1$ indicating losses due to reflection/transmission of light or incomplete charge collection. Using equation (10), idealised models for perovskites and organics were defined, with each having an optimistic $EQE_{max} = 0.9$. The resultant EQE_{PV} spectra are plotted for devices with $E_{opt} = 1.5\,eV$ in figure 2(a). In the idealised perovskite model a reasonable $E_U = 15\,meV$ was assumed [52], while in the idealised organic PV model $E_U = k_B T \approx 25.26\,meV$ was assumed as a reasonable minimum (with $T = 293.15\,K$) [28]. We note that in these idealised models there is a discontinuous jump in EQE_{PV} that is not present in real devices, with the transition between the exponential growth and saturation regimes generally being broadened by static energetic disorder [28, 57].

Using the three idealised models outlined above, the PCE was determined in the radiative, thermodynamic limit ($EQE_{EL} = 1$, $R_s = 0$, and $R_p \rightarrow \infty$) under LED-B4 illumination at $P_{source} = 0.3132\,mWcm^{-2}$ (corresponding to $L_{source} = 1000$ lux in photometric units), with the results illustrated as a function of optical bandgap (E_{opt}) in figure 2(b). From this figure, it is clear that a maximum PCE of 54% is predicted by the SQ model when $E_{opt} = 1.83$ eV. This maximum PCE decreases after accounting for losses in EQE_{max} and incorporating sub-gap absorption using equation (10); the former causes a 10% decrease in both J_{ph} and J_0 that reduces the maximum PCE down to 49%, while the latter induces additional losses in the open-circuit voltage that causes further loss in PCE [17]. In the perovskite model, a maximum PCE of around 48% is predicted. Whereas the maximum PCE is around 46% in the organic PV model (due to its larger Urbach energy). We stress that, as all these values were determined in the radiative limit, they will be further reduced by non-radiative losses in real devices.

A prominent source of voltage loss in some PV materials is the non-radiative recombination of excited charge carriers. In organic PVs the associated non-radiative open-circuit voltage (ΔV_{oc}^{nr}) loss has been observed to decrease with increasing E_{opt} via the so-called energy-gap law [58, 60, 61]. Figure 2(c) illustrates this trend using ΔV_{oc}^{nr} data determined experimentally for state-of-the-art systems, including data compiled by Ullbrich *et al* [58] alongside data previously compiled by the Authors [17, 59]. More recent ΔV_{oc}^{nr} data are shown by the more opaque data points in figure 2(c) (see supplementary note 2 for details) [31, 32, 62–92]. From this figure, it is clear that NFA organic PV blends typically have lower ΔV_{oc}^{nr} compared to FA blends, though such losses grow with decreasing E_{opt} in either case. To account for these intrinsic losses in the idealised organic PV model, ΔV_{oc}^{nr} is expressed empirically in terms of the optical gap as [59]

$$\Delta V_{oc}^{nr}(E_{opt}) = \Delta V_0 \left[\frac{\varepsilon - E_{opt}}{1 - \exp\left(-r\left[\varepsilon - E_{opt}\right]\right)} + \kappa \right] \tag{11}$$

where E_{opt} has units of eV, $\Delta V_0 = 0.57\,V\,eV^{-1}$, $\varepsilon = 1.49\,eV$, $r = 10\,eV^{-1}$, and $\kappa = 0.16\,eV$. We emphasise that equation (11) is simply an empirical model that captures trends observed in state-of-the-art devices. Models obtained using robust theoretical frameworks are available elsewhere [61, 93]. Using equation (11),
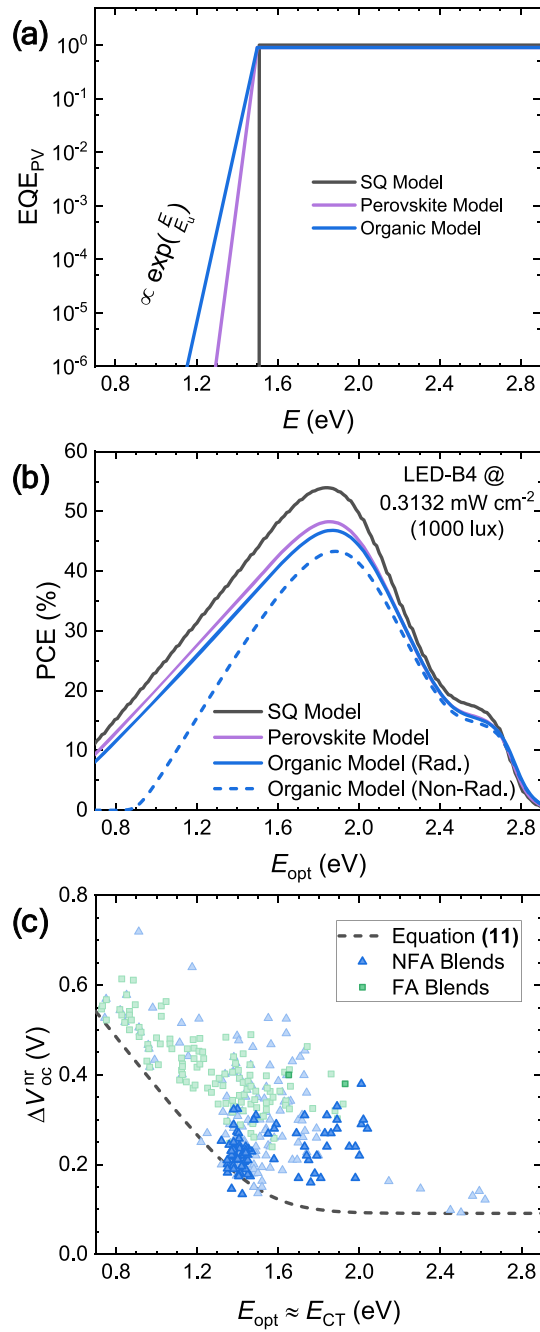
Figure 2. Comparing photovoltaic performance of different in different device models in the thermodynamic limit ($R_s = 0$; $R_p \rightarrow \infty$). (a) Photovoltaic external quantum efficiency (EQE_{PV}) spectra plotted as a function of photon energy (E) in three idealised device models, all with optical gap $E_{opt} = 1.50$ eV. Namely, these are the SQ model (black), the perovskite PV model (purple) with $EQE_{max} = 0.9$ and $E_U = 15$ meV, and the organic PV model (blue) with $EQE_{max} = 0.9$ and $E_U = k_B T = 25.26$ meV. (b) Power conversion efficiencies (PCEs) in the different device models under illumination by LED-B4 at irradiance $P_{source} = 0.3132$ mW cm^{-2} (corresponding to illuminance $L_{source} = 1000$ lux), where the radiative (non-radiative) limit of the organic PV model is indicated by the solid (dashed) blue curve. (c) Non-radiative open-circuit voltage losses (ΔV_{oc}^{nr}) in organic PVs, plotted against the energy of the charge-transfer state (E_{CT}), which is approximately equal to E_{opt} in low-offset organic PV blends such as those containing non-fullerene acceptors (NFAs). The lighter symbols indicate previously compiled data [17, 58, 59], while the darker blue triangles and green squares indicate additional, contemporary ΔV_{oc}^{nr} data for organic PV devices based on NFAs and fullerene acceptor (FA) systems, respectively (see supplementary note 2). The dashed black curve indicates the empirical model for ΔV_{oc}^{nr} defined in equation (11).

non-radiative open-circuit voltage losses were accounted for through the principle of reciprocity [47], with the electroluminescent external quantum efficiency (EQE_{EL}) written as

$$EQE_{EL} = \exp\left(-\frac{q\Delta V_{oc}^{nr}}{k_B T}\right). \tag{12}$$

Using equations (11) and (12), a non-radiative limit of the idealised organic PV model can be defined, with the resultant PCE under LED-B4 illumination indicated by the dashed blue curve in figure 2(b). From this figure, it is clear that incorporating non-radiative open-circuit voltage losses leads to further reduction in device performance, with a maximum PCE of 43% predicted in this model.

Of course, while the idealised, thermodynamic models considered in this section teach us what might be possible with fully-optimised devices, they teach us little about what real devices could currently achieve. Moreover, they do not account for other subtleties present in real, large-area PV devices, including geometric losses, point defects, and more. In the next section, we build on the findings presented here by considering the absorption properties of real devices.

2.3. Predicting indoor photovoltaic performance of devices measured under one-Sun conditions

To describe how real PV devices perform under indoor illumination conditions, we recently presented a technique for extrapolating measurements of devices made under one-Sun conditions to any set of illumination conditions [17]. This approach allows devices published in the literature to be recontextualised for indoor PV applications, without the additional expense of fabrication and/or the complexities of testing under several light sources. The technique utilises a device's EQE_{PV} spectrum and open-circuit voltage under one-Sun conditions ($V_{oc}^{\odot}$) to determine ΔV_{oc}^{nr} in the thermodynamic limit.

In figure 3 ultra-sensitive EQE_{PV} spectra are shown for a PM6:Y6 organic PV device [94] and a $Cs_{0.15}FA_{0.85}PbI_3$ perovskite PV device [95] in (a) and (b), respectively. An Urbach tail is present immediately below the gap in both systems, as indicated by the dashed blue lines, with $E_U \approx k_B T = 25\,meV$ for the PM6:Y6 device and $E_U \approx 13\,meV$ for the $Cs_{0.15}FA_{0.85}PbI_3$ device. We note that subtle deviations from perfectly exponential Urbach tails are likely the result of optical interference, due the thin-film PV devices acting as optical cavities [57, 96, 97]. Also indicated are the Gaussian absorption features of deep traps in the organic PV [28, 98, 99]. In the perovskite device, however, these sub-gap features appear exponential or like a broad Gaussian in nature, though the measurement becomes limited by thermal noise before the exact lineshape can be revealed [100].

A subtlety that must be accounted for when estimating ΔV_{oc}^{nr} from EQE_{PV} spectra is the weakly-absorbing features of deep trap states not obeying the standard reciprocity relation and generally not contributing to the thermodynamic limit [51, 94]. These features can in practice be truncated off the EQE_{PV} spectrum by introducing a lower limit ($E_{lower} > 0$) into the integrals of equations (5) and (6). The result of this analysis is indicated for the PM6:Y6 device in figure 3(c) and for the $Cs_{0.15}FA_{0.85}PbI_3$ device in figure 3(d), with the open-circuit voltage in the radiative limit (V_{oc}^{rad}) being simulated under AM1.5 G (one-Sun) conditions and plotted against E_{lower}. Note that $EQE_{EL} = 1$ is assumed in equation (6) to give the radiative limit, while a cell temperature $T = 293.15\,K$ is assumed throughout this work. For comparison, the open-circuit voltage determined experimentally under one-Sun conditions ($V_{oc}^{\odot}$) is indicated by the dashed lines, with $V_{oc}^{\odot} = 0.82V$ for the PM6:Y6 device and $V_{oc}^{\odot} = 1.02V$ for the $Cs_{0.15}FA_{0.85}PbI_3$ device [94, 95]. As E_{lower} decreases, more of the incident irradiance and device response is captured until V_{oc}^{rad} reaches a plateau. As E_{lower} is further reduced, the apparent V_{oc}^{rad} decreases again due to the presence of trap state absorption. For the $Cs_{0.15}FA_{0.85}PbI_3$ device, V_{oc}^{rad} ultimately drops below $V_{oc}^{\odot}$—a non-physical result that is an artifact of the deep trap states [94]. The device's non-radiative open-circuit voltage loss may be estimated from the difference between V_{oc}^{rad} and $V_{oc}^{\odot}$ at the plateau, giving $\Delta V_{oc}^{nr} = V_{oc}^{rad} - V_{oc}^{\odot} \approx 0.27V$ for the PM6:Y6 device, and $\Delta V_{oc}^{nr} \approx 0.23\,V$ for the $Cs_{0.15}FA_{0.85}PbI_3$ device. Assuming these values hold as a realistic lower limit of the non-radiative loss under any set of illumination conditions [17], then EQE_{EL} can be determined from the estimated ΔV_{oc}^{nr} using equation (12). Using this technique, a more accurate simulation of PV devices can be made in the non-radiative limit under indoor illumination conditions.

To demonstrate how the technique described above can be used to recontextualise measurements made under one-Sun conditions, the performance of several inorganic, perovskite, and organic devices stored in the PV-Simulator database were considered [38]. For reference, the reported performance of these systems under AM1.5 G conditions is indicated in figure 3(e) [39], with the highest PCE of 29.1% belonging to a gallium arsenide (GaAs) device [101]. Figure 3(f) shows the performance of the same systems simulated under LED-B4 illumination at irradiance $P_{source} = 0.3132\,mW\,cm^{-2}$, with many of the wider gap perovskite and organic PVs achieving higher PCEs than under AM1.5 G conditions. Through *in silico* analyses such as these, optimal PV materials for high performance under a variety of illumination conditions can be identified without needing to independently test every device under every light source.

In the remainder of this work, we focus our investigation on three PV devices: (i) a selenium-doped CdTe (cadmium telluride inorganic) device [102], (ii) a $MAPbI_3$ (perovskite) device [103]; and (iii) a PBDTTT-EFT:EH-IDTBR (organic) device [104]. To simplify notation, these three systems are herein
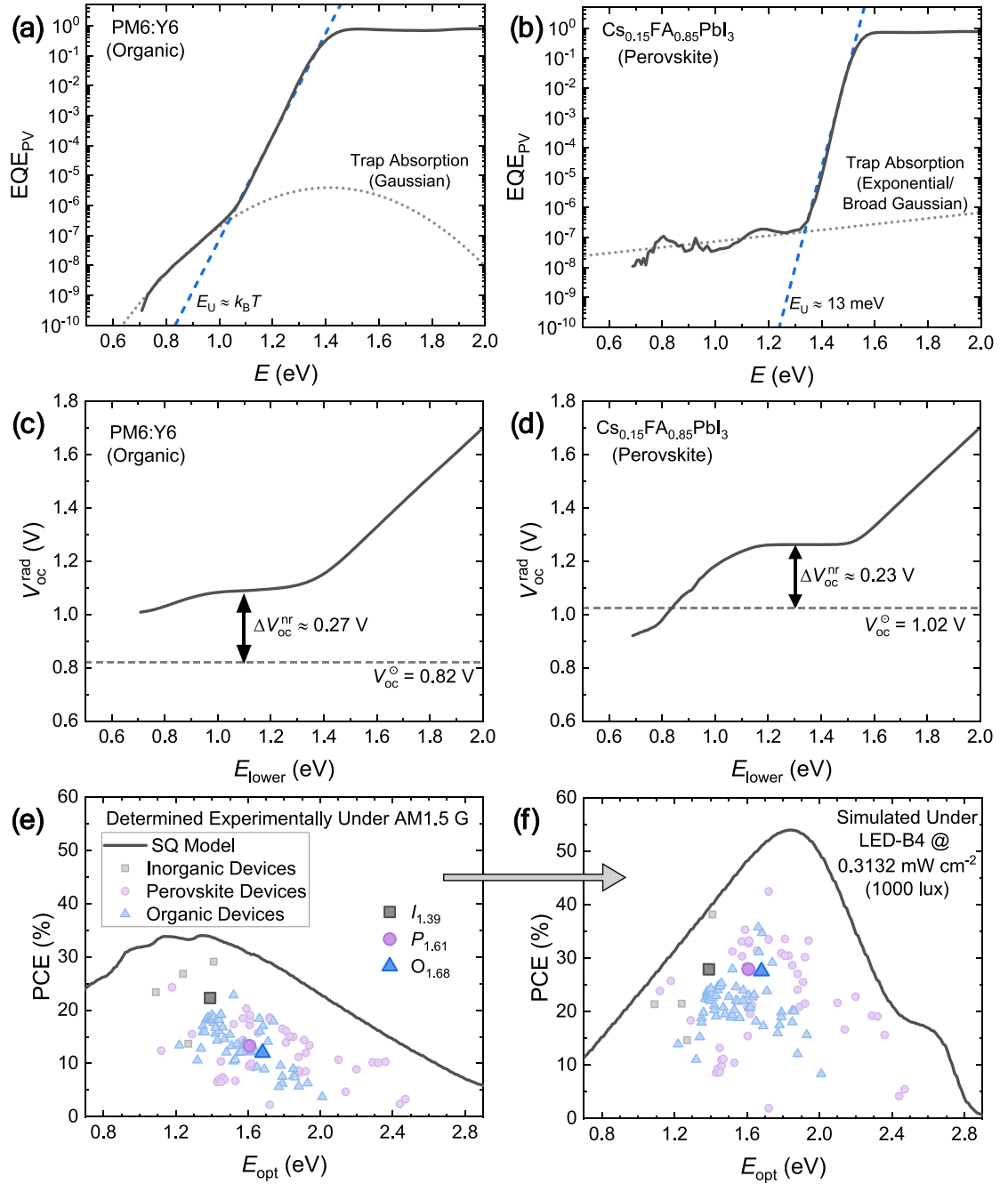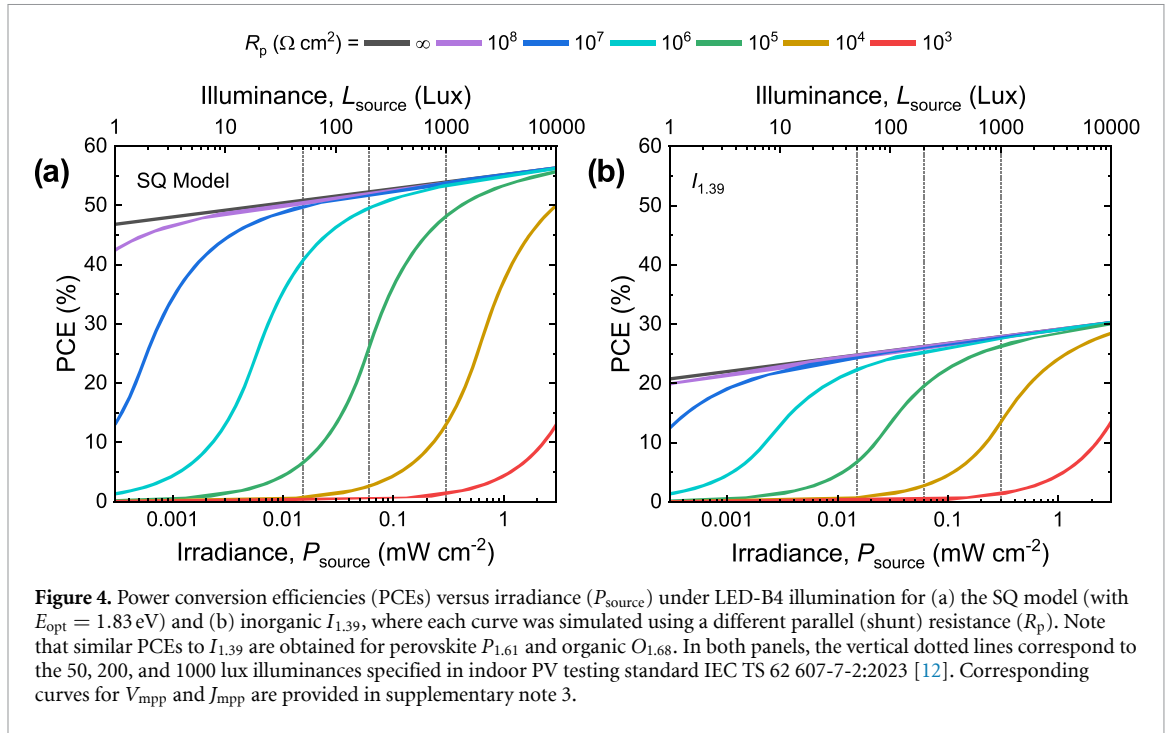
Figure 3. Extrapolating performance of devices measured under one-sun to indoor illumination conditions. Ultra-sensitive photovoltaic external quantum efficiency spectra for a PM6:Y6 (organic) [94] and a $Cs_{0.15}FA_{0.85}PbI_3$ (perovskite) [95] PV device are plotted versus photon energy (E) in (a) and (b), respectively. The regions where EQE_{PV} increases exponentially are indicated by the dashed blue lines, with the Urbach energy being $E_U \approx k_B T$ for PM6:Y6 and $E_U \approx 13\,meV$ for $Cs_{0.15}FA_{0.85}PbI_3$. In both panels, the absorption of deep trap states are indicated by the dotted lines with a Gaussian feature being present in (a) and an exponential/broad Gaussian feature being present in (b). (c) and (d) show the radiative open-circuit voltages (V_{oc}^{rad}) determined under AM1.5 G conditions for PM6:Y6 and $Cs_{0.15}FA_{0.85}PbI_3$, respectively, with the corresponding experimental open-circuit voltages ($V_{oc}^{\odot}$) indicated by the dashed lines. (e) The reported performance of several inorganic (grey squares), perovskite (purple circles), and organic (blue triangles) devices under AM1.5 G illumination, with the SQ limit included for reference [39]. (f) The performance of the systems in (e) simulated under LED-B4 illumination at irradiance $P_{source} = 0.3132\,mW\,cm^{-2}$ (corresponding to illuminance $L_{source} = 1000\,lux$ in photometric units). In (e) and (f) the systems $I_{1.39}$, $P_{1.61}$, and $O_{1.68}$ are indicated by the larger, more opaque symbols.

labelled according to their optical gap as $I_{1.39}$, $P_{1.61}$, and $O_{1.68}$, respectively, where 'I', 'P', and 'O' denote 'Inorganic', 'Perovskite' and 'Organic', respectively. These systems—which are illustrated by the darker symbols in figure 3(f)—were selected as they have similar predicted PCEs under LED-B4. However, as we will see shortly, PCE is not the sole figure-of-merit when considering PV modules for energy-harvesting applications, with parameters such as V_{mpp} having far-reaching implications when optimising module design.

Figure 4. Power conversion efficiencies (PCEs) versus irradiance (P_{source}) under LED-B4 illumination for (a) the SQ model (with $E_{opt} = 1.83\,\text{eV}$) and (b) inorganic $I_{1.39}$, where each curve was simulated using a different parallel (shunt) resistance (R_p). Note that similar PCEs to $I_{1.39}$ are obtained for perovskite $P_{1.61}$ and organic $O_{1.68}$. In both panels, the vertical dotted lines correspond to the 50, 200, and 1000 lux illuminances specified in indoor PV testing standard IEC TS 62 607-7-2:2023 [12]. Corresponding curves for V_{mpp} and J_{mpp} are provided in supplementary note 3.

2.4. Sensitivity to changes in illumination conditions

As previously highlighted, indoor PVs encounter a variety of illumination conditions, including different sources and light intensities. For example, order-of-magnitude variations in light intensities—from $0.01\,\text{mW cm}^{-2}$ to $1\,\text{mW cm}^{-2}$—can usually be encountered in most indoor spaces [8]. To show how this affects device performance, PCEs were simulated under LED-B4 illumination for a variety of shunt resistances, with the results plotted against the irradiance in figure 4. Note that the corresponding illuminances are indicated for reference, while additional curves indicating the irradiance-dependent behaviour of V_{mpp} and J_{mpp} are provided in supplementary note 3. Figure 4(a) shows the PCE in the SQ model (with $E_{opt} = 1.83\,\text{eV}$, i.e. the highest-PCE bandgap under LED-B4), whereas the PCE for $I_{1.39}$ is indicated in figure 4(b). Note that very similar PCE s are obtained for $P_{1.61}$ and $O_{1.68}$, as expected from figure 3(d). For reference, the 50, 200 and 1000 lux values specified in indoor PV testing standard IEC TS 62 607-7-2:2023 are indicated by the vertical dotted lines [12]. From this figure, it is clear that PCE grows logarithmically with irradiance in the case of infinite parallel (shunt) resistance ($R_p \rightarrow \infty$). A finite parallel resistance reduces PCE, with $R_p < 10^6\,\Omega\,\text{cm}^2$ (turquoise curves) limiting PV performance under typical indoor conditions. In all device models, PCE drops to near zero for $R_p \leq 10^4\,\Omega\,\text{cm}^2$ (red curves), indicating how a single cell's parallel resistance impacts its performance—a point we will return to in the context of PV modules in the next section.

As previously mentioned, the performance of indoor PVs needs to be considered under a variety of light sources. In figure 5, the thermodynamic-limit PCE, V_{mpp}, and J_{mpp} of the same three devices ($I_{1.39}$, $P_{1.61}$, and $O_{1.68}$) are compared under LED, FL lamp (FL), and standard solar light sources (where the typical irradiances have been used for the latter). For reference, the same figures-of-merit are indicated in the SQ model (with $E_{opt} = 1.83$ eV). In this investigation, the physical irradiance of each light source was fixed at $P_{source} = 0.3132\,\text{mW cm}^{-2}$ (corresponding to illuminance $L_{source} = 1000\,\text{lux}$ under LED-B4), meaning the perceived illuminance of each source would differ. While V_{mpp} is impervious to changes in light source, J_{mpp} is more sensitive and changes by up to 20% (for $O_{1.68}$), which in turn leads to variations in PCE of up to 8%. Consequently, indoor PVs optimised using a standard light source will likely perform differently under other light sources (and across different deployment locations).

3. Photovoltaic modules for energy-harvesting systems

With the performance of single-cell PVs based on real materials explored under a variety of indoor illumination conditions, we next focus on the integration of indoor PV modules into energy-harvesting systems. In the following discussions, we consider only the popular and often used e-peas® AEM13920 as an exemplar EHB. However, the method is universal and can be repeated for any EHB. Generally, the optimal number (N) of cells in a PV module for energy-harvesting systems will depend on its material composition,
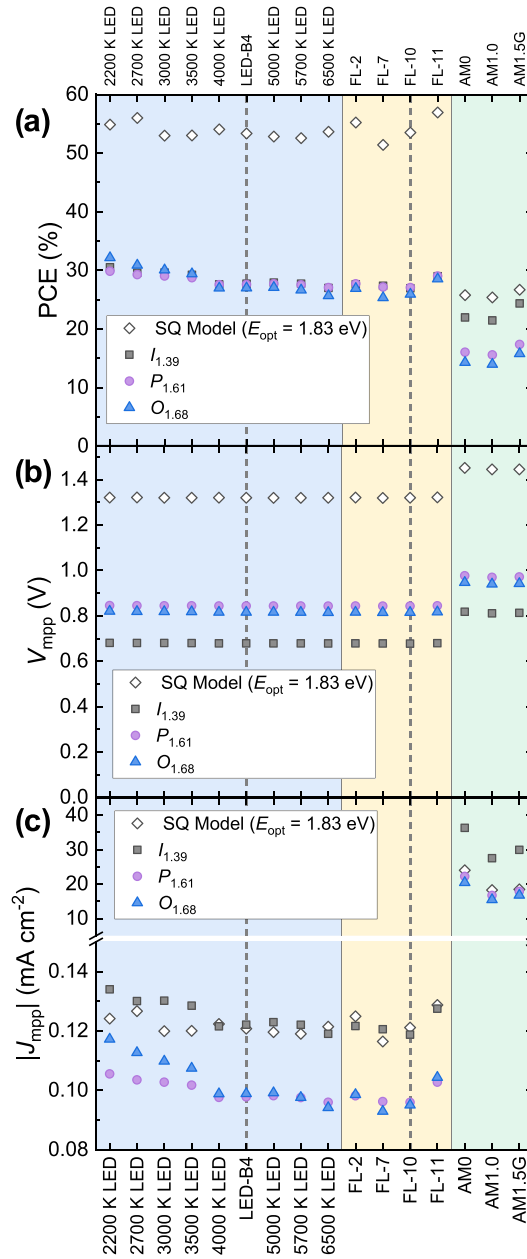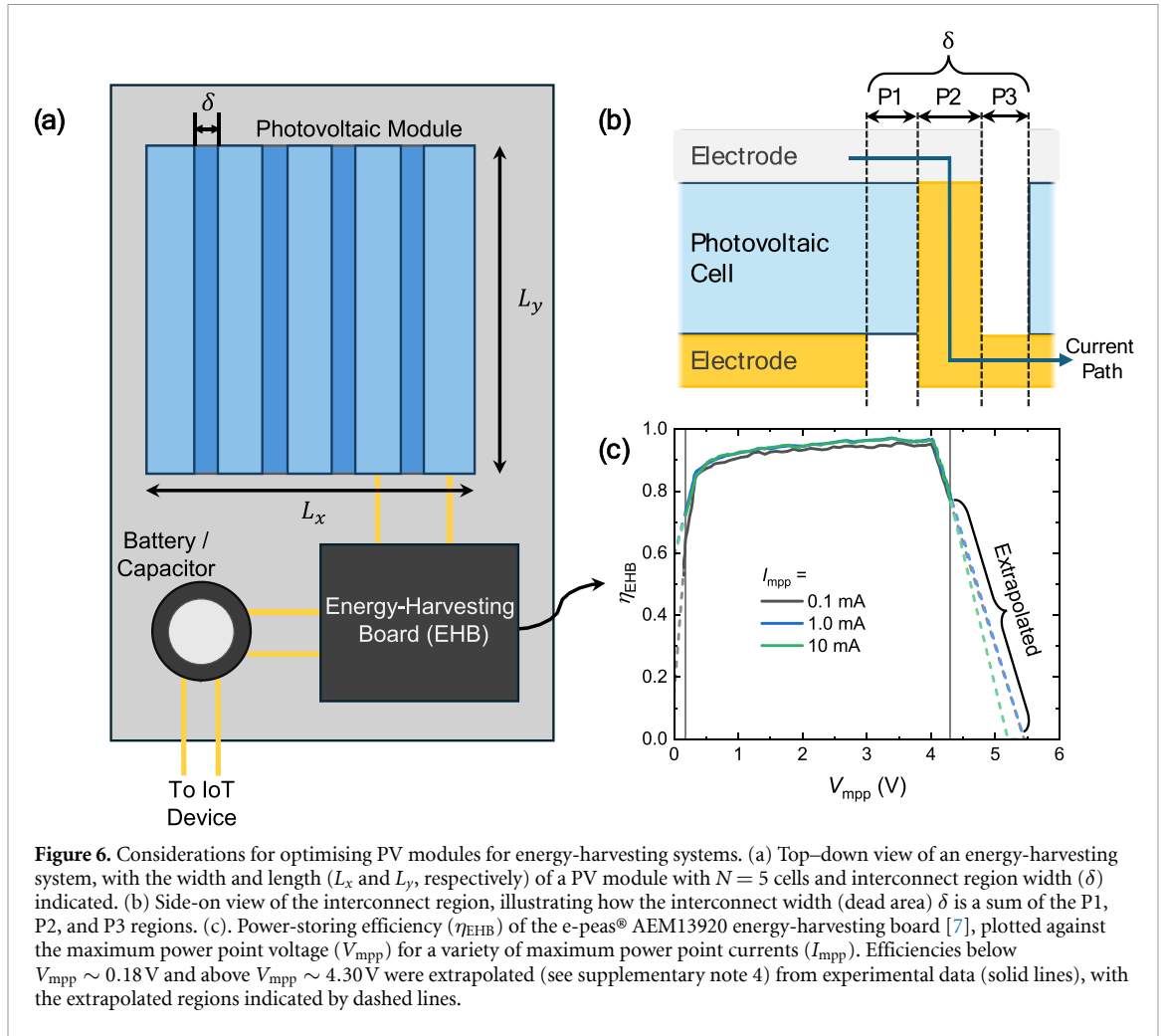
Figure 5. (a) PCE, (b) V_{mpp}, and (c) J_{mpp} of the SQ model (with $E_{opt} = 1.83$ eV) and three example systems under a variety of indoor light sources in the thermodynamic limit ($R_s = 0$; $R_p \rightarrow \infty$), where each has irradiance $P_{source} = 0.3132$ mW cm^{-2} (equivalent to illuminance $L_{source} = 1000$ lux under LED-B4). The standard solar spectra, on the other hand, have their usual irradiances, which are $P_{source} = 135.3$ mW cm^{-2} for AM0, $P_{source} = 104.0$ mW cm^{-2} for AM1.0, and $P_{source} = 100.3$ mW cm^{-2} for AM1.5 G. Data simulated for $I_{1.39}$, $P_{1.61}$, and $O_{1.68}$ are indicated by black squares, purple circles, and blue triangles, respectively. The corresponding performance in the SQ model (with $E_{opt} = 1.83$ eV) is indicated by the white diamonds.

the associated current-voltage characteristics, the scaling of point defects and shunt resistance with device area, the operational range of light intensities, and the chosen EHB.

3.1. Varying cell number in the thermodynamic limit

To increase the voltage generated by a PV device, a monolithic cell can be divided into several serially-connected cells to form a PV module. For inorganic semiconductor-based PVs this patterning can be done using photolithography. Whereas, for solution-processed PVs such as perovskites and organics, this is commonly done by fabricating a large-area device and singulating it into N cells. Assuming the final module has side lengths L_x and L_y, as illustrated in figure 6(a), then its total area is $A_{module} = L_x L_y$.

As the singulation process forms breaks in the top and bottom electrodes (labelled as P1 and P3 in figure 6(b), respectively), and also connects the top electrode of one cell to the bottom electrode of the next (P2), then 'interconnect' regions or 'dead areas' are formed between cells. These regions reduce the active area (or geometric fill factor) of the module, meaning less incident light is absorbed. The width of the

Figure 6. Considerations for optimising PV modules for energy-harvesting systems. (a) Top–down view of an energy-harvesting system, with the width and length (L_x and L_y, respectively) of a PV module with $N = 5$ cells and interconnect region width (δ) indicated. (b) Side-on view of the interconnect region, illustrating how the interconnect width (dead area) δ is a sum of the P1, P2, and P3 regions. (c). Power-storing efficiency (η_{EHB}) of the e-peas® AEM13920 energy-harvesting board [7], plotted against the maximum power point voltage (V_{mpp}) for a variety of maximum power point currents (I_{mpp}). Efficiencies below $V_{mpp} \sim 0.18\,V$ and above $V_{mpp} \sim 4.30\,V$ were extrapolated (see supplementary note 4) from experimental data (solid lines), with the extrapolated regions indicated by dashed lines.

interconnect region (δ)—being the sum of P1, P2, and P3—therefore needs to be as thin as possible. In this work, we assume $\delta = 100\,\mu m$ as a reasonable value for modules singulated using state-of-the-art laser scribing methods [35–37]. Assuming these interconnect regions run the entire length L_y of the PV module, the area of each cell (A_{cell}) can be written as

$$A_{cell} = \frac{A_{module} - (N-1) \times \delta \times L_y}{N}, \tag{13}$$

where the maximum number of cells for a given δ is constrained by $N_{max} < 1 + \frac{L_x}{\delta}$. If each of the N cells is identical and operates under the same illumination conditions (with no partial shading), then the total current of the module (I_{module}) is equal to the current of a single cell (I), giving

$$I_{module}(V_{module}) = I(V) = A_{cell} J(V), \tag{14}$$

where the current density $J(V)$ was defined in equation (4). On the other hand, the total voltage of the module is given by $V_{module} = NV_{cell}$. The product of this voltage and current yields the power generated by the module, which accounts for geometric losses via equation (13). By identifying the maximum power point of the module, its PCE can be determined.

In practice, not all of the power generated by the PV module will be stored by the energy-harvesting system. EHBs have some characteristic efficiency (η_{EHB}) that depends on the voltage and current output by the PV device. As previously stated, the efficiency of the energy-harvesting process is given by $\eta_{sys} = PCE \times \eta_{EHB}$, where PCE is that of the PV module. The efficiency of the exemplar EHB (e-peas® AEM13920) is illustrated in figure 6(c) [7]. While this particular EHB is quite resilient to orders-of-magnitude change in current (for $I_{module} > 0.1\,mA$), it is more sensitive to changes in voltage and operates best when the PV device produces between 3 V and 4 V. Beyond 4 V, this EHB goes over-voltage and can no longer store power efficiently. To describe the energy-harvesting system across a wider voltage range, the EHB efficiency was extrapolated (see supplementary note 4), with the result indicated by the dashed lines in figure 6(c). For
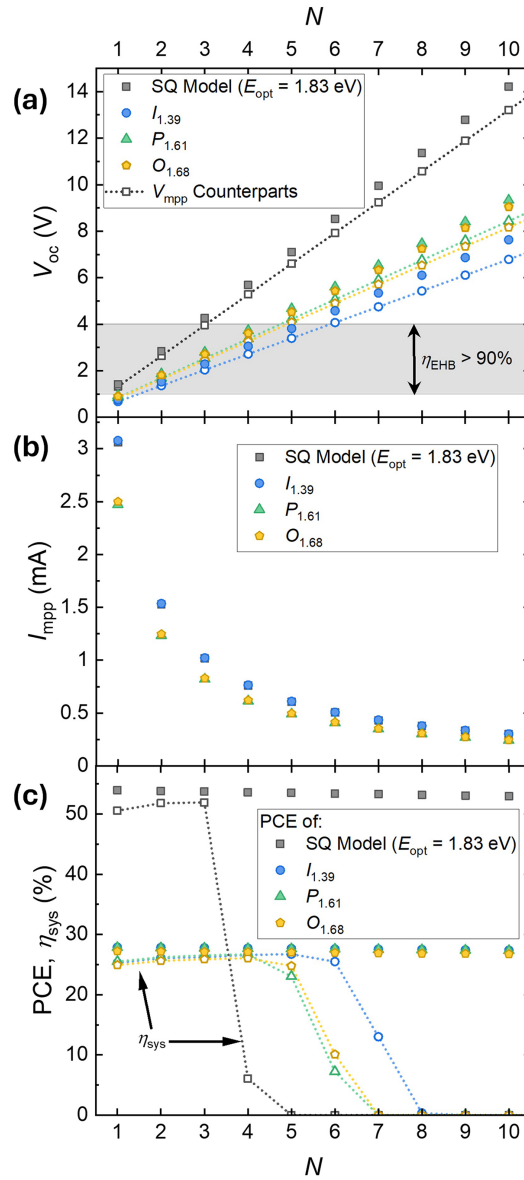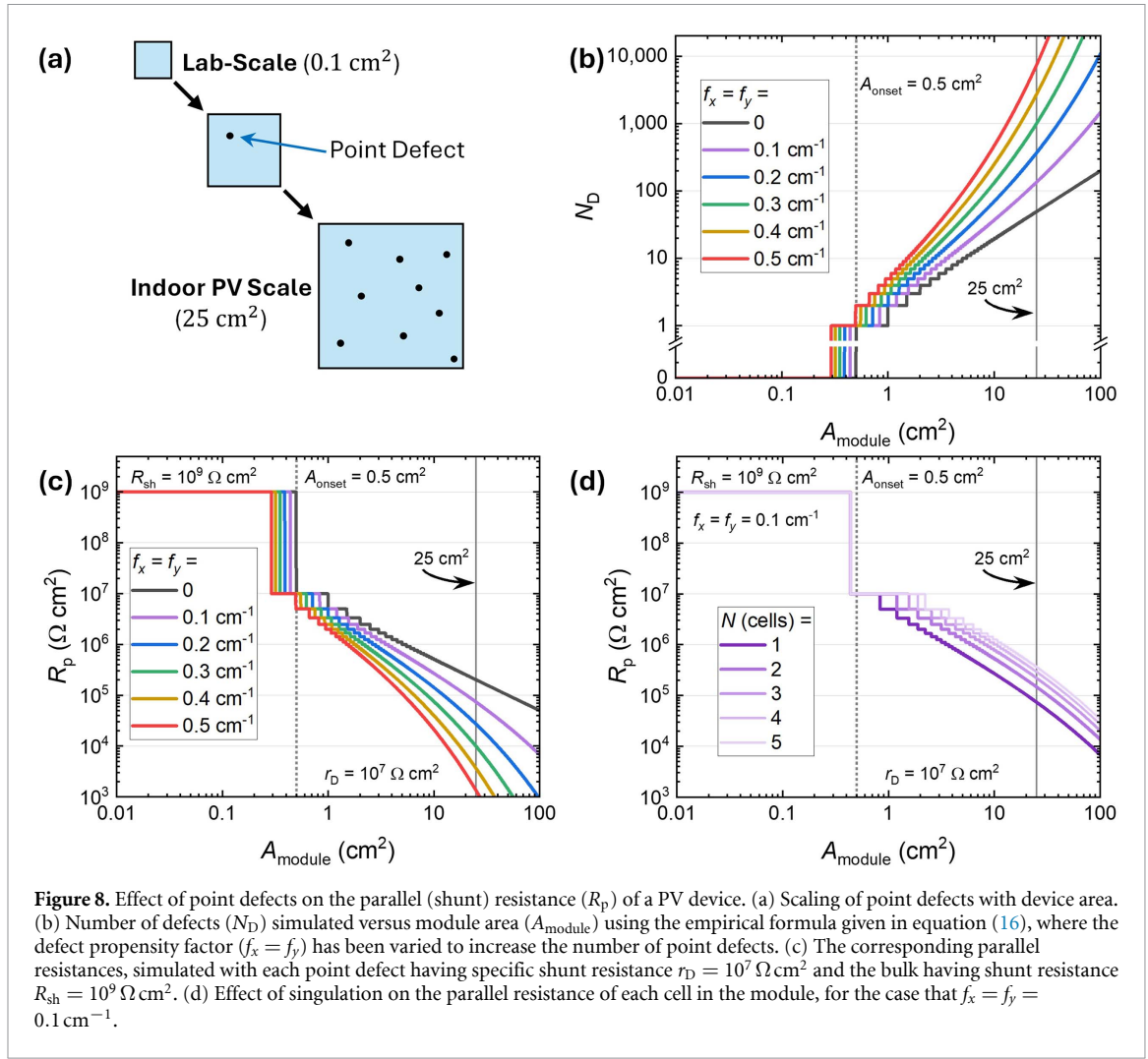
Figure 7. Photovoltaic figures-of-merit under LED-B4 illumination at irradiance $P_{source} = 0.3132\,\mathrm{mW\,cm^{-2}}$, simulated for $5\,\mathrm{cm} \times 5\,\mathrm{cm}$ PV modules as a function of the number of cells (N) using interconnect region width $\delta = 100\,\mu\mathrm{m}$. (a) Open-circuit voltage (V_{oc}) and maximum power point voltage (V_{mpp}) for four different device models, including the SQ model with $E_{opt} = 1.83\,\mathrm{eV}$ (black squares), and the three devices considered in section 2: $I_{1.39}$, $P_{1.61}$, and $O_{1.68}$, which are shown by the blue circles, green triangles, and yellow pentagons, respectively. The empty symbols connected by dotted lines indicate V_{mpp}. The grey shaded region indicates voltages at which $\eta_{EHB} > 90\%$. (b) Corresponding maximum power point current (I_{mpp}) of the same devices as a function of N. (c) Resultant PCEs and system efficiency (η_{sys}), which are shown by the filled-in and empty symbols (connected by dotted lines), respectively.

very small currents ($I_{module} < 0.1\,\mathrm{mA}$), the efficiency of this EHB may decrease considerably. Consequently, if at $P_{source} = 0.3132\,\mathrm{mW\,cm^{-2}}$ a monolithic ($N = 1$) PV cell produces current density $I \approx 0.1\,\mathrm{mA}$ per square centimetre (cf figure 5), then a reduction in light intensity must be matched by an equivalent increase in area to ensure efficient energy storing. Though, as previously mentioned, considerations such as these will closely depend on the chosen EHB.

With geometrical considerations established for scaling a single PV cell up to a PV module, we next considered the performance of the three state-of-the-art systems described in section 2 ($I_{1.39}$, $P_{1.61}$, and $O_{1.68}$). Figure 7 shows the results of the analysis for a $5\,\mathrm{cm} \times 5\,\mathrm{cm}$ PV module with interconnect width $\delta = 100\,\mu\mathrm{m}$ under LED-B4 illumination, where an irradiance $P_{source} = 0.3132\,\mathrm{mW\,cm^{-2}}$ was assumed (corresponding to illuminance $L_{source} = 1000\,\mathrm{lux}$) while the number of cells N was varied. For reference, the simulated result in the SQ model (at the optimal bandgap $E_{opt} = 1.83\,\mathrm{eV}$) is also included. Figure 7(a) shows the open-circuit voltage (V_{oc}) and maximum power point voltage (V_{mpp}), which grow linearly with N as expected, with the exact values depending on the chosen PV material, its bandgap, and its associated loss mechanisms.

Figure 8. Effect of point defects on the parallel (shunt) resistance (R_p) of a PV device. (a) Scaling of point defects with device area. (b) Number of defects (N_D) simulated versus module area (A_{module}) using the empirical formula given in equation (16), where the defect propensity factor ($f_x = f_y$) has been varied to increase the number of point defects. (c) The corresponding parallel resistances, simulated with each point defect having specific shunt resistance $r_D = 10^7 \, \Omega \, cm^2$ and the bulk having shunt resistance $R_{sh} = 10^9 \, \Omega \, cm^2$. (d) Effect of singulation on the parallel resistance of each cell in the module, for the case that $f_x = f_y = 0.1 \, cm^{-1}$.

As the interconnect width is small relative to the width of the module, geometric losses in current are likewise relatively small. As a result, the maximum power point current (I_{mpp}) shown in figure 7(b) is inversely proportional to N, which can be expected from equations (13) and (14) as $A_{cell} \propto 1/N$. In addition, the PCE of the module is mostly independent of N, as shown by the data points in figure 7(c). However, from the system efficiencies (η_{sys}) shown by the data points connected by dotted lines in the same panel, it is clear that while V_{mpp} increases with N, the energy-harvesting system eventually goes over-voltage (for the considered EHB) leading to a decrease in η_{EHB} and a resultant decrease in η_{sys}. Consequently, as the number of cells in the PV module increases, some optimum N is reached before η_{sys} drops rapidly to zero. This optimal N will depend on the type of material (and of course the type of EHB). For example, for inorganic $I_{1.39}$ the optimal N appears to be 5, whereas the optimal N for perovskite $P_{1.61}$, and organic $O_{1.68}$ appears to be 4 due to their wider-gaps and higher voltages. In other words, despite the three devices having similar PCEs under LED-B4 illumination (cf figure 4(d)), differences in V_{mpp} determine the optimal cell number. In the next sections, we explore how point defects and changes in illumination conditions can further influence the optimal cell number.

3.2. Scaling of point defects and parallel resistance in solution-processible photovoltaics

At the low light intensities characteristic of indoor settings, the parallel resistance (R_p in $\Omega \, cm^2$) is the dominant parasitic resistance limiting the performance of indoor PVs [5]. This total parallel resistance can be expressed in terms of the specific bulk shunt resistance of the PV material (R_{sh} in $\Omega \, cm^2$) and the specific shunt resistances of any point defects (r_D in $\Omega \, cm^2$) as [34]

$$\frac{1}{R_p} = \frac{1}{R_{sh}} + \sum_{i=1}^{N_D} \frac{1}{r_{D,i}}, \tag{15}$$

where N_D is the total number of point defects. For solution-processed perovskite and organic PVs, N_D generally scales with increasing device area, as illustrated in figure 8(a) [5]. To capture this behaviour, we have devised an empirical model to relate N_D to the module area; allowing us to probe the effect of point defects on the parallel resistance and performance of large-area modules.

In the empirical model, N_D has a linearly relationship with A_{module} for laboratory-scale areas ($A_{\text{module}} < 1 \, \text{cm}^2$). For practical-scale devices ($A_{\text{module}} > 10 \, \text{cm}^2$), however, this may not be the case. We therefore account for any higher-order relationships by relating N_D and A_{module} via

$$N_D = \left\lfloor \frac{A_{\text{module}}}{A_{\text{onset}}} \times e^{f_x L_x} \times e^{f_y L_y} \right\rfloor, \tag{16}$$

where the floor operation has been used to ensure $N_D \in \mathbb{Z}$. In this equation, the number of defects grows exponentially with the width and length of the device at large areas, with $f_{x(y)}$ being a point defect propensity factor along the width (length) of the PV module. These factors need not be equal, with fabrication techniques such as blade coating likely forming point defects anisotropically. On the other hand, A_{onset} quantifies the area at which point defects start to form. While equation (16) offers a convenient parameterisation of the number of defects, it is important to note that it is not based on any experimental observations. Instead, it is intended to connect R_p to A_{module} (via N_D). To better describe this relationship and validate the model, defect mapping and scanning techniques could be employed, though this is out of the scope of this work [105–107]. Generally, the parameters A_{onset}, f_x, and f_y will generally depend on the fabrication technique used to make the PV device and its associated variables. For solution-processible PVs, such variables can include coating-speed, solution viscosity, and temperature.

Using equation (16), the number of point defects and corresponding parallel resistance (for a monolithic cell) were simulated as a function of module area, assuming a reasonable $A_{\text{onset}} = 0.5 \, \text{cm}^2$, with the results illustrated in figures 8(b) and (c), respectively. From this figure, it is evident that the $f_x = f_y = 0$ case corresponds to a linear growth in defect density with module area, while $f_x = f_y > 0$ indicates exponentially more point defects forming for a given area. This in turn, lowers the total parallel shunt resistance of the device calculated using the parallel resistor model given by equation (15). To increase the parallel resistance, the effective number of point defects in a PV cell can be reduced by singulating a monolithic cell into a PV module, where the point defects are distributed amongst the cells. Figure 8(d) demonstrates this for a PV module of N cells in the case that $f_x = f_y = 0.1 \, \text{cm}^{-1}$ (assuming point defects are distributed evenly). By doing this, the number of point defects in each cell is reduced, and so its effective parallel resistance increases, which is vital for ensuring high performance under low light intensities. Singulation may also reduce Ohmic losses due to the series resistance of the electrodes, though these are less prominent at low light intensities.

3.3. Intensity-dependent system efficiencies

To optimise the design of PV modules for energy-harvesting applications across the full range of operating conditions, the behaviour of η_{sys} with changing light intensity must be considered. To this end, the system efficiencies $5 \, \text{cm} \times 5 \, \text{cm}$ PV modules based on the three systems considered so far ($I_{1.39}$, $P_{1.61}$, and $O_{1.68}$) were simulated under LED-B4 illumination as a function of irradiance, with the results plotted against in figure 9 alongside the system efficiency in the SQ model (with $E_{\text{opt}} = 1.83 \, \text{eV}$). In this figure, the number of cells in the module (N) was varied alongside the light intensity, with each cell being separated by interconnect width $\delta = 100 \, \mu\text{m}$. Furthermore, in all models the PV material has bulk shunt resistance $R_{\text{sh}} = 10^9 \, \Omega \, \text{cm}^2$, while the module has a total of $N_D = 100$ point defects (each with shunt resistance $r_D = 10^7 \, \Omega \, \text{cm}^2$) that are distributed evenly amongst multiple cells where applicable. We note that techniques used to process inorganic PVs such as $I_{1.39}$ are less prone to point defect formation than solution processible techniques (inorganic PVs are also generally thicker), and so the number of defects for this system would likely be lower. Therefore, in each panel the $N = 1$, $R_p \to \infty$ case has been indicated by the dashed line, which is more akin to the case for highly engineered commercial inorganic PV.

From figure 9, it is clear that at low light intensities the parallel resistance arising from the bulk shunt and point defects leads to a reduction in PCE and consequently η_{sys}. In all models this effect is most prominent in the case of a single monolithic cell ($N = 1$) as all point defects act in parallel. However, as the number of cells is increased the effective parallel resistance increases, leading to a higher η_{sys} at low light intensities. On the other hand, at high light intensities, modules with a large N go over-voltage, causing $\eta_{\text{sys}} \to 0$. Consequently, the optimal N for a PV module is dependent on the voltage-dependence of η_{EHB}, the exact range of illumination conditions, the associated current-voltage characteristics of the PV module, and the distribution and effective parallel resistance of any point defects. For example, between $0.01 \, \text{mW cm}^{-2}$ and $0.1 \, \text{mW cm}^{-2}$ (roughly 40 lux and 200 lux) a module based on $P_{1.61}$ with $N = 5$ cells will perform slightly better than a module with $N = 4$ cells. However, at $0.3 \, \text{mW cm}^{-2}$ (or 1000 lux), the $P_{1.61}$ module with $N = 5$
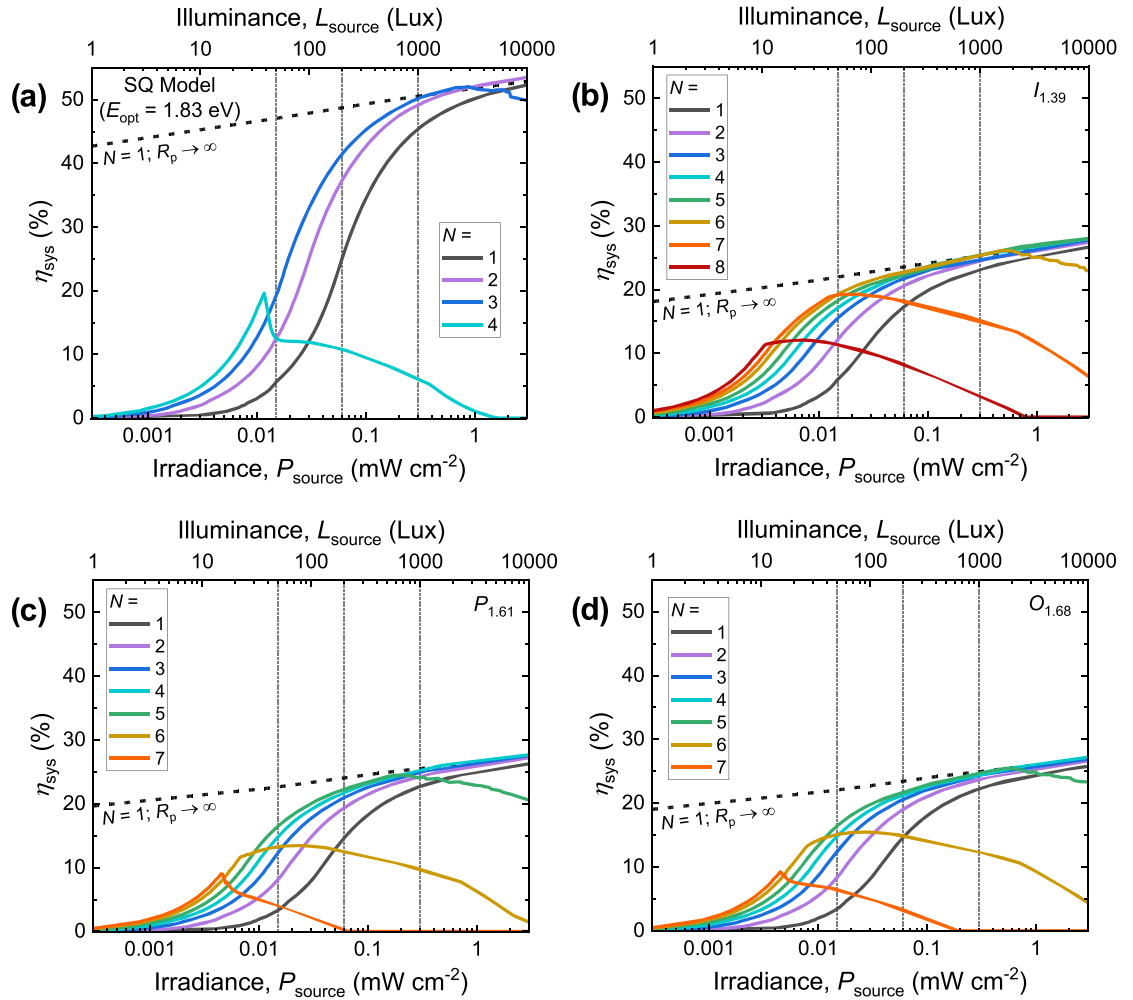
Figure 9. Irradiance-dependent system efficiency (η_{sys}) of $5\,\text{cm} \times 5\,\text{cm}$ PV modules based on (a) SQ model ($E_{opt} = 1.83\,\text{eV}$), (b) $I_{1.39}$, (c) $P_{1.61}$, and (d) $O_{1.68}$. In all models, $N_D = 100$ point defects are assumed across the whole module with each having a shunt resistance $r_D = 10^7\,\Omega\,\text{cm}^2$, while the bulk shunt resistance was assumed to be $R_{sh} = 10^9\,\Omega\,\text{cm}^2$. In all panels, the number of cells N was varied, assuming an interconnect width $\delta = 100\,\mu\text{m}$. In all panels/models the $N = 1$, $R_p \rightarrow \infty$ case is indicated by the dashed lines. Note that the vertical dotted lines indicate illuminances of 50, 200, and 1000 lux.

cells goes over-voltage and η_{sys} begins to decrease, meaning that $N = 4$ is more ideal for higher light intensities (again, for this specific EHB). Across the typical indoor range, $I_{1.39}$ has an optimal cell number $N = 5$ due to its narrower bandgap (and consequently lower V_{mpp}). Whereas for the wider-gap (and higher V_{mpp}) $P_{1.61}$, the optimal $N = 4$. Finally, despite having the widest gap, the various losses present in $O_{1.68}$ means that it requires $N = 5$ to achieve an optimal η_{sys}.

4. Case study: energy accumulated in a typical day

In our final investigation, the versatility of modules optimised in the previous section was probed using real-world irradiance data measured by Seunarine *et al* [9]. As illustrated in figure 10(a), ambient light conditions in internal spaces can fluctuate throughout the day, being characterised by daylight (or AM1.5 G irradiance filtered through a glass window) near noon, and by artificial light in the evening. Note that the original data was measured in August in a south-facing office. To consider a more arbitrary orientation and time of year, the highest light intensity (at 12 noon) was scaled to an irradiance $P_{source} = 0.3637\,\text{mW cm}^{-2}$ (corresponding to illuminance $L_{source} = 1000\,\text{lux}$), with all other spectra being scaled appropriately. We note that increasing or decreasing the light intensity will impact η_{sys}, as explored in the previous section. Of interest here is how the change in spectrum throughout the day impacts the efficiency of the energy-harvesting system.

Using the spectral irradiances plotted in figure 10(a), the power generated by $5\,\text{cm} \times 5\,\text{cm}$ PV modules based on the three materials considered so far (and the SQ Model with $E_{opt} = 1.83\,\text{eV}$) was determined, using
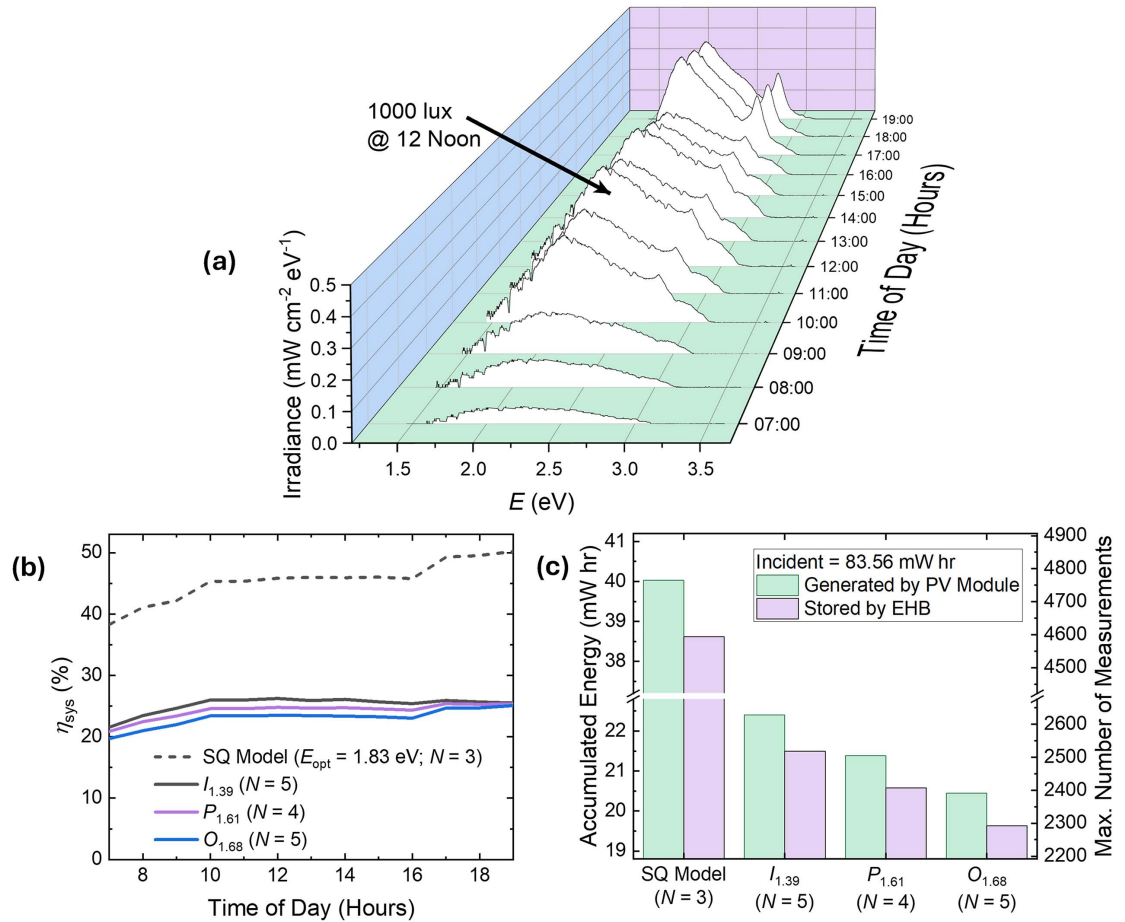
Figure 10. Accumulated energy generation and storage for an energy-harvesting system based on different PV materials, which have been simulated for a 12-hour period in an office with a south-facing window. (a) Spectral irradiance measured at hourly intervals, showing an interplay between daylight and artificial light throughout the day. Though the original spectra were measured in August [9], these spectra are normalised such that the highest measured illuminance during the day (at 12 noon) would be 1000 lux to better capture an average day. Using these irradiances, the (b) system efficiency and (c) accumulated energy generated and stored by energy-harvesting systems based on 5 cm × 5 cm PV modules was determined for the SQ model with $N = 3$ cells (and $E_{opt} = 1.83$ eV), $I_{1.39}$ with $N = 5$ cells, $P_{1.61}$ with $N = 4$ cells, and $O_{1.68}$ with $N = 5$ cells. Also indicated by the second vertical scale in (c) is the maximum number of daily measurements, which is determined from the stored energy (see supplementary note 5).

the optimal cell numbers identified in section 3; which were $N = 5$ for $I_{1.39}$ and $O_{1.68}$, and $N = 4$ for $P_{1.61}$. Note that interconnect width $\delta = 100\,\mu$m was assumed, with each module having bulk $R_{sh} = 10^9\,\Omega\,cm^2$ and $N_D = 100$ defects, each with specific shunt $r_D = 10^7\,\Omega\,cm^2$. The system efficiency of the four device models throughout the day is plotted in figure 10(b), where it has been assumed that the light intensity and spectrum measured on the hour is representative of the light intensity across the whole hour as a simplifying approximation. The total energy generated by the PV modules and stored by the EHB by the end of the day are shown in figure 10(c).

From figure 10, it is clear that only a fraction of the 83.56 mW hr energy incident on the module is actually stored, with the majority of power losses occurring in the PV cells (rather than through geometric fill factor losses or power-storing losses). Some of these losses are due to unabsorbed light or thermalisation, which can be mitigated using multi-junction approaches [46, 108], at the cost of higher fabrication expense likely not justified for the economics of indoor light harvesting for IoT. Nevertheless, most of the energy generated by the PV modules is stored by the EHBs, with $I_{1.39}$ providing the most energy and $O_{1.68}$ providing the least.

To give some context as to how the energies stored by the different systems translate to real-world IoT sensors, a second vertical scale representing maximum number of daily measurements was provided in figure 10(c). Here a reasonable power consumption was assumed per duty cycle to determine the maximum number of transmissions per day from the stored energy (see supplementary note 5). From this it is clear that an extra few hundred measurements could be made in a typical day by selecting one PV module over another. Thus, by considering the various illumination conditions real devices will encounter, including whether or not some sunlight is present at a given location within a room, the choice of PV materials, module design,

EHB, and required communication frequency can be optimised to achieve higher efficiency energy-harvesting and communication systems.

5. Concluding remarks

In conclusion, we have explored the effects of singulation on the performance of PV modules based on current and next-generation semiconductor materials. We have shown how various loss mechanisms present in PV materials, including sub-gap absorption, non-radiative open-circuit voltage losses, parasitic resistances, and point defects, can influence the optimal design of PV modules for energy-harvesting applications. By considering a variety of light sources and intensities, we have probed the versatility of these devices across many typical indoor lighting conditions while showing why the photometric units of lux are unreliable for device characterisation. Despite some materials having a lower V_{mpp} and PCE due to intrinsic losses, we have shown that high energy-harvesting efficiencies can still be achieved by increasing the number of cells in a PV module (with the caveat of increased fabrication cost and complexity). However, some foresight of the deployment location is required to fully optimise the module design. In practice, this means that the application of the IoT device and the associated illumination conditions must be considered when designing the PV module.

To support the findings presented in this work, we have expanded our PV-Simulator tool to include capabilities for simulating indoor PV module-based energy-harvesting systems [38]. Under any desired light source and intensity, this tool and its associated database can be used to compare the performance of hundreds of different material systems, encompassing thin-film inorganics, perovskites, and organics. Future work could include optimising the design of energy-harvesting systems for particular lighting conditions, whether that be a singular device that performs well across all light sources, or different devices tailored for different categories of light sources—such as, e.g. a system optimised for 4000 K to 6000 K LEDs. Following this, techno-economic analyses could be performed to determine which PV materials offer the cheapest and most environmentally-friendly routes to realising a fully-fledged IoT.

Data availability statement

The data used to simulate the findings presented in this work are available online with the PV-Simulator tool [38]. The data used to prepare the figures are available at the following URL: https://github.com/Austin-M-Kay/Data.

Conflicts of Interest

The Authors declare no conflicts of interest.

ORCID iDs

Austin M Kay ⬤ https://orcid.org/0000-0002-9126-5340
Shimra N Ahmed ⬤ https://orcid.org/0009-0000-9985-3246
Nicholas Burridge ⬤ https://orcid.org/0000-0001-9570-5748
Drew B Riley ⬤ https://orcid.org/0000-0001-6688-0694
Ardalan Armin ⬤ https://orcid.org/0000-0002-6129-5354
Oskar J Sandberg ⬤ https://orcid.org/0000-0003-3778-8746
Zaid Haymoor ⬤ https://orcid.org/0000-0001-6606-307X
Matthew J Carnie ⬤ https://orcid.org/0000-0002-4232-1967

Paul Meredith ⬤ https://orcid.org/0000-0002-9049-7414

Gregory Burwell ⬤ https://orcid.org/0000-0002-2534-9626

References

[1] Vermesan O, Friess P, Guillemin P, Giaffreda R, Grindvoll H, Eisenhauer M, Serrano M, Moessner K, Spirito M and Blystad L-C 2022 Internet of things beyond the hype: research, innovation and deployment *Ecosystems and Markets* (River Publishers) pp 15–118

[2] Alsamhi S H, Ma O, Ansari M and Meng Q 2019 Greening internet of things for greener and smarter cities: a survey and future prospects *Telecommun. Syst.* **72** 609–32

[3] Zeadally S, Shaikh F K, Talpur A and Sheng Q Z 2020 Design architectures for energy harvesting in the internet of things *Renew. Sustain. Energy Rev.* **128** 109901

[4] Blakesley J C *et al* 2025 Roadmap on photovoltaic absorber materials for sustainable energy conversion *J. Phys. Energy* **6** 041501

[5] Burwell G, Sandberg O J, Li W, Meredith P, Carnie M and Armin A 2022 Scaling considerations for organic photovoltaics for indoor applications *Sol. RRL* **6** 2200315

[6] Pecunia V, Occhipinti L G and Hoye R L Z 2021 Emerging indoor photovoltaic technologies for sustainable internet of things *Adv. Energy Mater.* **11** 2100698

[7] e-peas AEM13920—dual input energy harvesting (available at: https://e-peas.com/product/aem13920-dual-source-energy-harvesting/) (28th January 2024)

[8] Grandhi G K *et al* 2025 Promises and challenges of indoor photovoltaics *Nat. Rev. Clean Technol.* **1** 132–47

[9] Seunarine K, Haymoor Z, Spence M, Burwell G, Kay A, Meredith P, Armin A and Carnie M 2024 Light power resource availability for energy harvesting photovoltaics for self-powered IoT *J. Phys. Energy* **6** 015018

[10] Zeiske S, Meredith P, Armin A and Burwell G 2023 Importance of spectrally invariant broadband attenuation of light in indoor photovoltaic characterization *APL Energy* **1** 026103

[11] Parsons D, Koutsourakis G and Blakesley J 2024 Performance measurements for indoor photovoltaic devices: classification of a novel light source *APL Energy* **2** 016110

[12] International Electrotechnical Commission (IEC) 2023 Indoor testing standard 62607-7-2:2023 (available at: https://webstore.iec.ch/publication/61819)

[13] CIE 2018 Relative spectral power distributions of illuminants representing typical fluorescent lamps, 1nm Wavelength Steps (available at: https://cie.co.at/datatable/relative-spectral-power-distributions-illuminants-representing-typical-fluorescent-lamps-0)

[14] CIE 2018 Relative spectral power distributions of illuminants representing typical LED lamps, 1nm spacing (available at: https://cie.co.at/datatable/relative-spectral-power-distributions-illuminants-representing-typical-led-lamps-1nm)

[15] Freunek M, Freunek M and Reindl L M 2012 Maximum efficiencies of indoor photovoltaic devices *IEEE J. Photovoltaics* **3** 59–64

[16] Lübke D, Hartnagel P, Angona J and Kirchartz T 2021 Comparing and quantifying indoor performance of organic solar cells *Adv. Energy Mater.* **11** 2101474

[17] Kay A M, Fitzsimons M E, Burwell G, Meredith P, Armin A and Sandberg O J 2023 The thermodynamic limit of indoor photovoltaics based on energetically-disordered molecular semiconductors *Sol. RRL* **7** 2300277

[18] Burwell G, Zeiske S, Caprioglio P, Sandberg O J, Kay A M, Farrar M D, Kim Y R, Snaith H J, Meredith P and Armin A 2024 Wide-gap perovskites for indoor photovoltaics *Sol. RRL* **8** 2400180

[19] Green M A, Dunlop E D, Yoshita M, Kopidakis N, Bothe K, Siefer G and Hao X 2024 Solar cell efficiency tables (version 63) *Prog. Photovolt., Res. Appl.* **32** 3–13

[20] Almora O *et al* 2023 Device performance of emerging photovoltaic materials (version 3) *Adv. Energy Mater.* **13** 2203313

[21] Armin A *et al* 2021 A history and perspective of non-fullerene electron acceptors for organic solar cells *Adv. Energy Mater.* **11** 2003570

[22] Datt R, Caprioglio P, Choudhary S, Lan W, Snaith H and Tsoi W C 2024 Engineered charge transport layers for improving indoor perovskite photovoltaic performance *J. Phys. Energy* **6** 025014

[23] Abbel R, Galagan Y and Groen P 2018 Roll-to-roll fabrication of solution processed electronics *Adv. Eng. Mater.* **20** 1701190

[24] Burkitt D, Patidar R, Greenwood P, Hooper K, McGettrick J, Dimitrov S, Colombo M, Stoichkov V, Richards D and Beynon D 2020 Roll-to-roll slot-die coated p–i–n perovskite solar cells using acetonitrile based single step perovskite solvent system *Sustain. Energy Fuels* **4** 3340–51

[25] Søndergaard R R, Hösel M and Krebs F C 2013 Roll-to-roll fabrication of large area functional organic materials *J. Polym. Sci. B* **51** 16–34

[26] Patidar R, Burkitt D, Hooper K, Richards D and Watson T 2020 Slot-die coating of perovskite solar cells: an overview *Mater. Today Commun.* **22** 100808

[27] Wong J, Omelchenko S T and Atwater H A 2020 Impact of semiconductor band tails and band filling on photovoltaic efficiency limits *ACS Energy Lett.* **6** 52–57

[28] Kaiser C, Sandberg O J, Zarrabi N, Li W, Meredith P and Armin A 2021 A universal Urbach rule for disordered organic semiconductors *Nat. Commun.* **12** 3988

[29] Englman R and Jortner J 1970 The energy gap law for radiationless transitions in large molecules *Mol. Phys.* **18** 145–64

[30] Fu J, Yang Q, Huang P, Chung S, Cho K, Kan Z, Liu H, Lu X, Lang Y and Lai H 2024 Rational molecular and device design enables organic solar cells approaching 20% efficiency *Nat. Commun.* **15** 1830

[31] Fu J *et al* 2023 19.31% binary organic solar cell and low non-radiative recombination enabled by non-monotonic intermediate state transition *Nat. Commun.* **14** 1760

[32] Sun Y *et al* 2024 π-extended nonfullerene acceptor for compressed molecular packing in organic solar cells to achieve over 20% efficiency *J. Am. Chem. Soc.* **146** 12011–9

[33] Chen H *et al* 2025 Organic solar cells with 20.82% efficiency and high tolerance of active layer thickness through crystallization sequence manipulation *Nat. Mater.* **24** 444–53

[34] Meredith P and Armin A 2018 Scaling of next generation solution processed organic and perovskite solar cells *Nat. Commun.* **9** 5261

[35] Flick A C, Rolston N and Dauskardt R H 2024 Indirect liftoff mechanism for high-throughput, single-source laser scribing for perovskite solar modules *Adv. Energy Mater.* **14** 2303175

[36] Schultz C, Fenske M, Dagar J, Zeiser A, Bartelt A, Schlatmann R, Unger E and Stegemann B 2020 Ablation mechanisms of nanosecond and picosecond laser scribing for metal halide perovskite module interconnection–an experimental and numerical analysis *Sol. Energy* **198** 410–8

[37] Taheri B, De Rossi F, Lucarelli G, Castriotta L A, Di Carlo A, Brown T M and Brunetti F 2021 Laser-scribing optimization for sprayed SnO_2-based perovskite solar modules on flexible plastic substrates *ACS Appl. Energy Mater.* **4** 4507–18

[38] Kay A M 2025 Photovoltaic performance simulator (PV-simulator) (available at: https://github.com/Austin-M-Kay/Photovoltaic_Performance_Simulator)

[39] Almora O *et al* 2025 Device performance of emerging photovoltaic materials (version 5) *Adv. Energy Mater.* **15** 2404386

[40] Sudevalayam S and Kulkarni P 2010 Energy harvesting sensor nodes: survey and implications *IEEE Commun. Surv. Tutor.* **13** 443–61

[41] Cree-LED Cree-LED X-lamp (R) LEDs (available at: www.cree-led.com/products/leds/xlamp/)

[42] Sze S M, Li Y and Ng K K 2021 *Physics of Semiconductor Devices* 4th edn (Wiley)

[43] CIE 2019 CIE spectral luminous efficiency for photopic vision (available at: https://cie.co.at/datatable/cie-spectral-luminous-efficiency-photopic-vision)

[44] Cui Y, Hong L, Zhang T, Meng H, Yan H, Gao F and Hou J 2021 Accurate photovoltaic measurement of organic cells for indoor applications *Joule* **5** 1016–23

[45] Cui Y, Hong L and Hou J 2020 Organic photovoltaic cells for indoor applications: opportunities and challenges *ACS Appl. Mater. Interfaces* **12** 38815–28

[46] Nelson J A 2003 *The Physics of Solar Cells* (Imperial College Press)

[47] Rau U 2007 Reciprocity relation between photovoltaic quantum efficiency and electroluminescent emission of solar cells *Phys. Rev. B* **76** 085303

[48] Würfel P 1982 The chemical potential of radiation *J. Phys. C* **15** 3967

[49] Shockley W and Queisser H J 1961 Detailed balance limit of efficiency of p-n junction solar cells *J. App. Phys.* **32** 510–9

[50] Urbach F 1953 The long-wavelength edge of photographic sensitivity and of the electronic absorption of solids *Phys. Rev.* **92** 1324

[51] Zarrabi N, Sandberg O J, Meredith P and Armin A 2023 Subgap absorption in organic semiconductors *J. Phys. Chem. Lett.* **14** 3174–85

[52] Zeiske S, Sandberg O J, Zarrabi N, Wolff C M, Raoufi M, Peña-Camargo F, Gutierrez-Partida E, Meredith P, Stolterfoht M and Armin A 2022 Static disorder in lead halide perovskites *J. Phys. Chem. Lett.* **13** 7280–5

[53] Wu X, Trinh M T, Niesner D, Zhu H, Norman Z, Owen J S, Yaffe O, Kudisch B J and Zhu X-Y 2015 Trap states in lead iodide perovskites *J. Am. Chem. Soc.* **137** 2089–96

[54] Chantana J, Kawano Y, Nishimura T, Mavlonov A and Minemoto T 2020 Impact of Urbach energy on open-circuit voltage deficit of thin-film solar cells *Sol. Energy Mater. Sol. Cells* **210** 110502

[55] Li M, Huang P and Zhong H 2023 Current understanding of band-edge properties of halide perovskites: Urbach tail, rashba splitting, and exciton binding energy *J. Phys. Chem. Lett.* **14** 1592–603

[56] Ščajev P, Mekys A, Subačius L, Stanionytė S, Kuciauskas D, Lynn K G and Swain S K 2022 Impact of dopant-induced band tails on optical spectra, charge carrier transport, and dynamics in single-crystal CdTe *Sci. Rep.* **12** 12851

[57] Kay A M, Sandberg O J, Zarrabi N, Li W, Zeiske S, Kaiser C, Meredith P and Armin A 2022 Quantifying the excitonic static disorder in organic semiconductors *Adv. Funct. Mater.* **32** 2113181

[58] Ullbrich S *et al* 2019 Emissive and charge-generating donor–acceptor interfaces for organic optoelectronics with low voltage losses *Nat. Mater.* **18** 459–64

[59] Kay A M, Riley D B, Sandberg O J, Burwell G, Meredith P and Armin A 2024 On the performance limits of agrivoltaics—from thermodynamic to geo-meteorological considerations *Sol. RRL* **8** 2400456

[60] Benduhn J *et al* 2017 Intrinsic non-radiative voltage losses in fullerene-based organic solar cells *Nat. Energy* **2** 17053

[61] Azzouzi M, Yan J, Kirchartz T, Liu K, Wang J, Wu H and Nelson J 2018 Nonradiative energy losses in bulk-heterojunction organic photovoltaics *Phys. Rev. X* **8** 031055

[62] Sun Z *et al* 2024 Insight into designing high-performance polythiophenes for reduced Urbach energy and nonradiative recombination in organic solar cells *Adv. Funct. Mater.* **34** 2403093

[63] Wu H *et al* 2024 Decreasing exciton dissociation rates for reduced voltage losses in organic solar cells *Nat. Commun.* **15** 2693

[64] Lai S *et al* 2024 Impact of electrostatic interaction on vertical morphology and energy loss in efficient pseudo-planar heterojunction organic solar cells *Adv. Mater.* **36** 2313105

[65] Jiang X, Wang X, Wang Y, Ran G, Liu W, Lu H, Li H, Wei N, Wei Z and Lin Y 2024 Achieving 19.78%-efficiency organic solar cells by 2D/1A ternary blend strategy with reduced non-radiative energy loss *Adv. Funct. Mater.* **34** 2406744

[66] Cui X, Ran G, Lu H, Liu Y, Jiang H, Zhang H, Li D, Liu Y, Lin Y and Ma Z 2024 Enabling low nonradiative recombination losses in organic solar cells by efficient exciton dissociation *Adv. Funct. Mater.* **34** 2400219

[67] Ren J *et al* 2024 Optimizing molecular packing via steric hindrance for reducing non-radiative recombination in organic solar cells *Angew. Chem., Int. Ed.* **63** e202406153

[68] Xin J *et al* 2024 Elucidate the thermal degradation mechanism of Y6-based organic solar cells by establishing structure-property correlation *Adv. Energy Mater.* **14** 2401433

[69] Yang S, Chen Z, Zhu J, Yang D, Wang H, Ding P, Wu J, Yan P, Xie L and Chen F 2024 Guest acceptors with lower electrostatic potential in ternary organic solar cells for minimizing voltage losses *Adv. Mater.* **36** 2401789

[70] Pan J, Guan J, Wang Z, Zhang R, Fu Y, Yu X, Zhang Q and Han Y 2024 Alleviating excessive aggregation of a non-fullerene acceptor by delaying and shortening the crystallization time to reduce the energy loss of ternary organic solar cells *J. Mater. Chem. C* **12** 4142–56

[71] Song J *et al* 2024 Non-halogenated solvent-processed organic solar cells with approaching 20% efficiency and improved photostability *Angew. Chem., Int. Ed.* **63** e202404297

[72] Xiang H, Sun F, Zheng X, Gao B, Zhu P, Cong T, Li Y, Wang X and Yang R 2024 Tackling energy loss in organic solar cells via volatile solid additive strategy *Adv. Sci.* **11** 2401330

[73] Bai Y *et al* 2024 Multi-selenophene strategy enables dimeric acceptors-based organic solar cells with over 18.5% Effic. *Adv. Energy Mater.* **14** 2400938

[74] He X, Qi F, Zou X, Li Y, Liu H, Lu X, Wong K S, Jen A K-Y and Choy W C 2024 Selenium substitution for dielectric constant improvement and hole-transfer acceleration in non-fullerene organic solar cells *Nat. Commun.* **15** 2103

[75] Li D *et al* 2024 Halogenated nonfused ring electron acceptor for organic solar cells with a record efficiency of over 17% *Adv. Mater.* **36** 2310362

[76] Zhu Y *et al* 2024 Suppressing exciton-vibration coupling to prolong exciton lifetime of nonfullerene acceptors enables high-efficiency organic solar cells *Angew. Chem., Int. Ed.* **63** e202316227

[77] An N *et al* 2020 Solution-processed organic solar cells with high open-circuit voltage of 1.3 V and low non-radiative voltage loss of 0.16 V *Adv. Mater.* **32** 2002122

[78] Wang J, Ma L, Lee Y W, Yao H, Xu Y, Zhang S, Woo H Y and Hou J 2021 Design of ultra-high luminescent polymers for organic photovoltaic cells with low energy loss *Chem. Commun.* **57** 9132–5

[79] Gao B, Yao H, Hong L and Hou J 2019 Efficient organic solar cells with a high open-circuit voltage of 1.34 V *Chin. J. Chem.* **37** 1153–7

[80] Wang J *et al* 2023 A wide bandgap acceptor with large dielectric constant and high electrostatic potential values for efficient organic photovoltaic cells *J. Am. Chem. Soc.* **145** 13686–95

[81] Casademont-Viñas M, Capolat D, Quesada-Ramírez A, Reinfelds M, Trimmel G, Sanviti M, Martín J, Goñi A R, Kirchartz T and Campoy-Quiles M 2024 Combinatorial screening of wide band-gap organic solar cell materials with open-circuit voltage between 1.1 and 1.4 V *J. Mater. Chem. A* **12** 16716–28

[82] Jeon J, Hosoya S, Saito M, Osaka I, Ohkita H and Kim H D 2024 Photon energy loss in ternary polymer solar cells based on nonfullerene acceptor as a third component *Battery Energy* **3** 20240011

[83] Thapa G J, Chauhan M, Mauthe J P, Dougherty D B and Amassian A 2024 Mapping interfacial energetic landscape in organic solar cells reveals pathways to reducing nonradiative losses (arXiv:2406.11735)

[84] Lee J-W, Sun C, Phan T N-L, Lee D C, Tan Z, Jeon H, Cho S, Kwon S-K, Kim Y-H and Kim B J 2023 Trimerized small-molecule acceptors enable high-performance organic solar cells with high open-circuit voltage and prolonged life-time *Energy Environ. Sci.* **16** 3339–49

[85] Hosseini S M, Wilken S, Sun B, Huang F, Jeong S Y, Woo H Y, Coropceanu V and Shoaee S 2023 Relationship between energetic disorder and reduced recombination of free carriers in organic solar cells *Adv. Energy Mater.* **13** 2203576

[86] Zhang Y, Yuan S, Zhang C, Ding C, Zhang C and Xu H 2023 Mitigating the trade-off between non-radiative recombination and charge transport to enable efficient ternary organic solar cells *Materials* **16** 5620

[87] Shen Q *et al* 2023 Progressive evolutions of non-fused ring electron acceptors toward efficient organic solar cells with improved photocurrent and reduced energy loss *Chem. Eng. J.* **471** 144472

[88] Suthar R, Dahiya H, Singh A K, Sharma G D and Karak S 2023 Role of exciton lifetime, energetic offsets, and disorder in voltage loss of bulk heterojunction organic solar cells *ACS Appl. Mater. Interfaces* **15** 3214–23

[89] Yang K, Chang Y, Chang Y, Lyu K and Wei Z 2023 Mechanisms and strategies to reduce energy loss in non-fullerene organic solar cells *J. Funct. Polym.* **36** 321–39

[90] Jia Z *et al* 2023 Near-infrared absorbing acceptor with suppressed triplet exciton generation enabling high performance tandem organic solar cells *Nat. Commun.* **14** 1236

[91] Kaienburg P, Bristow H, Jungbluth A, Habib I, McCulloch I, Beljonne D and Riede M 2023 Vacuum-deposited donors for low-voltage-loss nonfullerene organic solar cells *ACS Appl. Mater. Interfaces* **15** 31684–91

[92] Liu B *et al* 2023 Double-cable conjugated polymers based on simple non-fused electron acceptors for single-component organic solar cells *Macromolecules* **56** 1154–64

[93] Chen X-K *et al* 2021 A unified description of non-radiative voltage losses in organic solar cells *Nat. Energy* **6** 799–806

[94] Zarrabi N, Sandberg O J, Zeiske S, Li W, Riley D B, Meredith P and Armin A 2020 Charge-generating mid-gap trap states define the thermodynamic limit of organic photovoltaic devices *Nat. Commun.* **11** 5567

[95] Othman M *et al* 2024 Alleviating nanostructural phase impurities enhances the optoelectronic properties, device performance and stability of cesium-formamidinium metal–halide perovskites *Energy Environ. Sci.* **17** 3832–47

[96] Armin A, Zarrabi N, Sandberg O J, Kaiser C, Zeiske S, Li W and Meredith P 2020 Limitations of charge transfer state parameterization using photovoltaic external quantum efficiency *Adv. Energy Mater.* **10** 2001828

[97] Kaiser C, Zeiske S, Meredith P and Armin A 2020 Determining ultralow absorption coefficients of organic semiconductors from the sub-bandgap photovoltaic external quantum efficiency *Adv. Opt. Mater.* **8** 1901542

[98] Vandewal K, Tvingstedt K, Gadisa A, Inganäs O and Manca J V 2009 On the origin of the open-circuit voltage of polymer–fullerene solar cells *Nat. Mater.* **8** 904–9

[99] Vandewal K, Tvingstedt K, Gadisa A, Inganäs O and Manca J V 2010 Relating the open-circuit voltage to interface molecular properties of donor:acceptor bulk heterojunction solar cells *Phys. Rev. B* **81** 125204

[100] Zeiske S, Kaiser C, Meredith P and Armin A 2020 Sensitivity of sub-bandgap external quantum efficiency measurements of solar cells under electrical and light bias *ACS Photonics* **7** 256–64

[101] Green M A, Dunlop E D, Siefer G, Yoshita M, Kopidakis N, Bothe K and Hao X 2022 Solar cell efficiency tables (version 61) *Prog. Photovolt., Res. Appl.* **31** 3–16

[102] Mallick R *et al* 2023 Arsenic-doped Cdsete solar cells achieve world record 22.3% efficiency *IEEE J. Photovolt.* **13** 510–5

[103] Cai Q *et al* 2018 Enhancing efficiency of planar structure perovskite solar cells using Sn-doped TiO$_2$ as electron transport layer at low temperature *Electrochimica Acta* **261** 227–35

[104] Baran D *et al* 2018 Robust nonfullerene solar cells approaching unity external quantum efficiency enabled by suppression of geminate recombination *Nat. Commun.* **9** 2059

[105] Hentz O, Singh A, Zhao Z and Gradečak S 2019 Visualizing nonradiative mobile defects in organic–inorganic perovskite materials *Small Methods* **3** 1900110

[106] Breitenstein O, Bauer J, Altermatt P P and Ramspeck K 2010 Influence of defects on solar cell characteristics *Solid State Phenom.* **156** 1–10

[107] Wang J, Bi L, Fu Q and Jen A K Y 2024 Methods for passivating defects of perovskite for inverted perovskite solar cells and modules *Adv. Energy Mater.* **14** 2401414

[108] Hirst L C and Ekins-Daukes N J 2011 Fundamental losses in solar cells *Prog. Photovolt., Res. Appl.* **19** 286–93